TU Delft

Delft University of Technology

The effect of pH on the corrosion protection of aluminum alloys in lithium-carbonate-containing NaCl solutions

Michailidou, E.; Visser, P.; Mol, J.M.C.; Kosari, A.; Terryn, H.A.; Baert, K.; Gonzalez Garcia, Y.

DOI
10.1016/j.corsci.2022.110851

Publication date
2023

Document Version
Final published version

Published in
Corrosion Science

Citation (APA)
Michailidou, E., Visser, P., Mol, J. M. C., Kosari, A., Terryn, H. A., Baert, K., & Gonzalez Garcia, Y. (2023). The effect of pH on the corrosion protection of aluminum alloys in lithium-carbonate-containing NaCl solutions. *Corrosion Science*, *210*, Article 110851. https://doi.org/10.1016/j.corsci.2022.110851

Important note
To cite this publication, please use the final published version (if applicable).
Please check the document version above.

Copyright
Other than for strictly personal use, it is not permitted to download, forward or distribute the text or part of it, without the consent of the author(s) and/or copyright holder(s), unless the work is under an open content license such as Creative Commons.

Takedown policy
Please contact us and provide details if you believe this document breaches copyrights.
We will remove access to the work immediately and investigate your claim.

This work is downloaded from Delft University of Technology.
For technical reasons the number of authors shown on this cover page is limited to a maximum of 10.

Corrosion Science 210 (2023) 110851

Contents lists available at ScienceDirect

Corrosion Science

journal homepage: www.elsevier.com/locate/corsci

The effect of pH on the corrosion protection of aluminum alloys in lithium-carbonate-containing NaCl solutions

E. Michailidou [a,b,*], P. Visser [b], J.M.C. Mol [a], A. Kosari [a], H. Terryn [c], K. Baert [c], Y. Gonzalez-Garcia [a]

[a] Delft University of Technology, Department of Materials Science and Engineering, Mekelweg 2, 2628CD Delft, the Netherlands
[b] AkzoNobel, Rijksstraatweg 31, 2171AJ Sassenheim, the Netherlands
[c] Vrije Universiteit Brussel, Group of Electrochemistry and Surface Engineering (SURF), Pleinlaan 2, 1050 Brussels, Belgium

ARTICLE INFO

Keywords:
Aluminium
Lithium carbonate
Potentiodynamic polarisation
Raman Spectroscopy
SEM
Passivation

ABSTRACT

The corrosion inhibiting effect of lithium carbonate has been studied over the pH range relevant for atmospheric corrosion conditions at the polymer/metal interface. It is demonstrated that lithium carbonate offers optimum corrosion protection under moderately alkaline conditions attributed to the formation of a protective layer identified as aluminum-lithium layered double hydroxide. It is proposed that an active-to-passive transition occurs in the presence of lithium carbonate under moderately alkaline conditions where anodic dissolution of the aluminum matrix is an important step prior to the formation of the protective layer. After prolonged exposure, the protective layer is uniformly formed on the surface of AA2024-T3 and lithium containing AA2198-T8 covering both the matrix and active intermetallic particles thus hindering further corrosion reactions.

1. Introduction

Various studies have shown that lithium salts offer an effective and irreversible corrosion protection of organic coated AA2024-T3 under neutral salt spray conditions [1–5]. In the presence of a through-coating defect, the lithium salts are able to leach from the organic coating matrix to the exposed metal substrate and it is suggested that this leaching phenomenon increases the pH of the bulk electrolyte in the coating defect to moderately alkaline conditions (i.e. pH 9–10) [4–6]. The increase of the bulk electrolyte pH is attributed to the chemical dissociation of the lithium carbonate. The Li^+ aquo-cation does not hydrolyze readily[7], however the carbonate ions (CO_3^{2-} $pK_b = 3.75$) act as a conjugate base that can then combine with a proton to form hydrogen carbonate (HCO_3^-) and hydroxyl ions (OH^-) are formed as a result of water dissociation during reaction 1 [8].

$$CO_3^{2-} + H_2O \rightleftharpoons HCO_3^- + OH^- \quad (1)$$

Due to the elevated pH and the presence of aggressive anions to the bulk electrolyte, the aluminum matrix dissolves to form a lithium intercalated and hydrated aluminum(hydr)oxide layer offering corrosion protection at the defect site [5,6,9]. The typical morphology of the formed protective layer on AA2024-T3 alloy in the presence of lithium salts is a three-layer structure composed of an inner dense region, an intermediate porous region and an outer columnar region [4,10–12]. The chemical composition of each structure has been identified as pseudoboehmite, lithium containing pseudoboehmite and Al-Li layered double hydroxide (LDH) accordingly [12]. However, variations of the typical protective layer morphology have been reported within a through-coating defect attributed to local lithium concentration distribution, local anodic and cathodic processes and local pH variations [10,12]. It is reported that for a scribed lithium-containing organic coating exposed to neutral salt spray test, the local pH within the scribe increases to approximately 9–10 and a lithium containing pseudoboehmite protective layer is formed adjacent to the organic coating [5]. At later stages of neutral salt spray exposure, it is reported that the lithium containing pseudoboehmite is converted to LDH which phenomenon is attributed to further local pH increase, possibly pH 11–13, and higher concentration of lithium being leached from the organic coating as a function of time [12,13]. Lastly, the selective growth of LDH layer is reported closer to the center of the scribe at longer neutral salt spray exposure times which observation is attributed to the local alloy heterogeneity with local cathodic and anodic activities [10,12].

The passivation of aluminum and its alloys in the presence of lithium salts by a continuous surface film under alkaline conditions has been

* Corresponding author at: AkzoNobel, Rijksstraatweg 31, 2171AJ Sassenheim, the Netherlands.
E-mail address: emmanouela.michailidou@akzonobel.com (E. Michailidou).

https://doi.org/10.1016/j.corsci.2022.110851
Received 17 August 2022; Received in revised form 21 October 2022; Accepted 18 November 2022
Available online 20 November 2022
0010-938X/© 2022 The Authors. Published by Elsevier Ltd. This is an open access article under the CC BY license (http://creativecommons.org/licenses/by/4.0/).

extensively reported in literature [13–18] and it is suggested that the conditions for the protective layer formation are satisfied adequately in alkaline solutions where pH > 10 [13]. However, under atmospheric corrosion conditions the local pH may vary from pH 1–2 to alkaline pH [19]. In the corrosion front, the local pH is strongly acidic due to the stepwise aluminum aquo-cation hydrolysis mechanism and the local release of protons, whereas in the cathodic region alkaline conditions dominate the local pH as a result of the oxygen reduction reaction [19–21]. However, it is practically difficult to determine the exact value at the cathodic site of the filament head due to low liquidity [22]. Consequently, it is important to investigate the corrosion inhibition efficiency of lithium salts at the pH range established during atmospheric corrosion conditions in order to understand and define the conditions required at the penetrative coating defect site for the inhibitor to provide optimum corrosion protection.

Additional interest is taken in the corrosion protection of the third-generation aerospace grade aluminum-lithium alloys in the presence of lithium salts. The third-generation aluminum-lithium alloys contain 2–4 wt% Cu and 1–2 wt% Li in which the lithium additions to aluminum alloys result into 3% density reduction and 6% increase in Young's modulus which is beneficiary in aerospace applications where high specific strength and stiffness at low density is required [23–25]. For AA2198-T8, which is the aluminum-lithium alloy under investigation in this paper, the mechanical properties are reported as 503 MPa for ultimate tensile strength and 455 MPA for tensile yield strength [23]. Furthermore, the third generation of aluminum-lithium alloys show enhanced fracture toughness characteristics, increased crack growth resistance and the anisotropy of the mechanical properties has been significantly reduced compared to the previous generations [24–28]. Consequently, the third generation of aluminum-lithium alloys is considered a potential replacement for the conventional aerospace AA2024-T3 alloy [28,29].

However, it is well known that the corrosion of both AA2024-T3 [30–32] and AA2198-T8 [17,33–36] in aqueous chloride electrolytes is highly localized and that often more than one form of localized corrosion is observed such as pitting, crevices and intergranular attack. The mechanical strength of AA2024-T3 is derived by the addition of Cu in the bulk metal composition which leads to the formation of secondary intermetallic phase particles [37]. However, the presence of Cu rich particles enhances the electrocatalytic activity of the cathodic oxygen reduction reaction [38] and it is the galvanic coupling between the secondary intermetallic phase particles and the aluminum matrix that makes AA2024-T3 highly susceptible to localized corrosion [38]. In the case of AA2198-T8, the major strengthening phase is considered to be the T1 (Al_2CuLi) phase which tends to preferentially precipitate at dislocations in the aluminum matrix [36,39,40]. It has been shown in prior works that the T1 phase is highly anodic with respect to the surrounding aluminum matrix exhibiting a high corrosion rate in aqueous chloride electrolytes [17] and the highly deformed grains are the most prone to localized corrosion [33,34]. Initially, the T1 phase undergoes active anodic dissolution leading to the selective leaching of the Li and Al species and a Cu-rich residue [35,36]. As a result, the particle becomes cathodic with respect to the aluminum matrix thus promoting the anodic dissolution of the surrounding matrix [33,34].

The present paper aims to investigate the importance of pH and define the optimal pH range on the corrosion protection of aluminum-based substrates in the presence of lithium carbonate. The aluminum substrates under investigation are the legacy AA2024-T3 and third-generation aluminum-lithium AA2198-T8 alloys. Their electrochemical response in terms of potentiodynamic polarization has been recorded in a selected range of pH buffered chloride containing solutions in the presence of lithium carbonate. Consequently, the corrosion protection offered by lithium carbonate is determined through the systematic pH variation of the bulk electrolyte. Additionally, the time- and location-resolved corrosion and the morphology and chemical composition of the protective layer formed on both alloys under investigation have been characterized via in-situ time-lapse microscopy, scanning electron microscopy (SEM) and Raman spectroscopy.

2. Experimental

2.1. Materials

AA2198-T8 and AA2024-T3 samples were provided by Arconic and were cut into 3 × 3 cm square coupons of 2 mm and 1 mm thickness respectively. Both alloys' nominal chemical composition is presented in Table 1. The sample surface was prepared using silicon carbide polishing pads (Struers) with alcohol-based lubricant (DP-Lubricant, Struers) used during the process. The polishing order was ascending from grit 80 to grit 4000 followed by cleaning the samples in an ultrasonic bath in ethanol for 5 min and drying under flowing nitrogen gas. All the chemicals used were of analytical grade provided by the Sigma-Aldrich Chemical Company. All glassware equipment was cleaned thoroughly using 2 M HCl (aq) followed by rinsing with distilled water.

2.2. Methods

All experiments were performed in aerated conditions and in contact with the room atmosphere at 20 °C in 10^{-1} M aqueous NaCl electrolyte buffered at systematically varied pH from pH 2 to pH 13 unless otherwise stated. The buffering agents used are listed in Table 2. In all cases the stoichiometry of the selected chemical species was taken into consideration and the concentration of the Cl^- aquo-anions was kept constant at 10^{-1} M. For near-marine and marine atmospheric settings it is reported that deliquesced water layers contain high concentrations of sea salt in which the predicted brine composition for halite varies from 1 to 10 molality as a function of relative humidity and concentration [41]. Upon evaporation, the brine is rich in Na^+ and Cl^- until halite precipitation occurs for which the predicted concentration is reported at 10^{-1} M [41]. For the lithium carbonate containing solutions, 10^{-2} M Li_2CO_3 was added to the bulk electrolyte which concentration is reported to provide similar protective layer to what is observed within a defect area of a lithium leaching protective coating [6].

2.2.1. Potentiodynamic polarization

The electrochemical measurements were conducted in freshly prepared electrolyte in a conventional three-electrode cell using a BioLogic VSP-300 Multi-Potentiostat and EC-Lab collection software. The reference electrode was a saturated Ag/AgCl electrode, and a platinum mesh was used as counter electrode. The sample was masked with 90 μm thick extruded PTFE 5490 tape (3 M Ltd) leaving a circular exposed area of 8 mm diameter and was exposed for 30 min to bulk electrolyte under open circuit potential conditions (OCP). Following OCP, potentiodynamic polarization was performed at a sweep rate of 0.1 mV/s over a range of 1 V vs OCP. In all cases, both anodic and cathodic polarizations were performed separately, and all measurements were repeated three times. The EC-lab software provided by BioLogic was used to fit the polarization curves for Tafel analysis using the Stern equation through which the corrosion current (i_{corr}) was approximated.

2.2.2. In-situ time-lapse microscopy

The corrosion mechanism of AA2024-T3 and AA2198-T8 in the absence and presence of lithium carbonate was studied by in-situ time-lapse microscopy as reported by Sullivan et al. [42] to investigate the influence of the inhibitor on the visual appearance of propagating corrosion features. The sample under investigation was covered with 90 μm thick extruded PTFE 5490 tape (3 M Ltd) leaving a circular exposed area of 0.5 mm diameter which was achieved using a biopsy needle. The sample was secured within the petri dish using an arrangement of double-sided tape and PTFE tape. A Leica optical microscope was used to observe the sample under in-situ conditions. A submersible cap with a thin microscope glass window was used as a

Table 1
Chemical composition of commercial AA2198-T8 and AA2024-T3 aluminum alloy.

Chemical Composition (%) of AA2198-T8											
Si	Fe	Cu	Mn	Mg	Cr	Ni	Zn	Ti	Zr	Ag	Li
0.02	0.04	3.4	83*	0.32	10*	30*	86*	0.03	0.11	0.26	1.0
Others: Each: 0.05% max, Total: 0.15% max, Aluminum: Remainder, *ppm											

Chemical Composition (%) of AA2024-T3								
Si	Fe	Cu	Mn	Mg	Cr	Zn	Ti	Others
0.5	0.5	3.8–4.9	0.3–0.9	1.2–1.8	0.1	0.25	0.15	0.15
Aluminum: Remainder								

Table 2
Chemical composition of the pH buffering agents.

pH	Buffering Agents
2	0.2 M Potassium Chloride (KCl)
	0.2 M Hydrochloric Acid (HCl)
4	0.1 M Acetic Acid (CH_3COOH)
	0.1 M Sodium Acetate Tri-hydrate ($CH_3COONa{\cdot}3\ H_2O$)
7	0.1 M Tris(hydroxymethyl)aminomethane ($NH_2C(CH_2OH)_3$)
	0.1 M Hydrochloric Acid (HCl)
10	0.025 M Sodium Tetraborate ($Na_2B_4O_7{\cdot}10\ H_2O$)
	0.1 M Sodium Hydroxide (NaOH)
13	0.2 M Potassium Chloride (KCl)
	0.2 M Sodium Hydroxide (NaOH)

protective cover for the objective lens to prevent contamination and damage. The petri dish was filled with 250 ml of freshly prepared 10^{-1} M aqueous NaCl electrolyte in the presence and absence of 10^{-2} M Li_2CO_3 in the selected pH range and the optical focus was adjusted to clear in-situ images of the exposed sample area. Digital images were taken at a 1 min time interval over 24 h of total experimental time using the time-lapse function incorporated on the Infinity I camera (Lumera corporation) attached to the microscope lens. Due to the laborious nature of in-situ time-lapse microscopy single measurements were taken per selected condition. Digital image analysis was performed using ImageJ.

2.2.3. Scanning electron microscopy

FIB/SEM cross-sectioning was carried out by means of a Thermo-Fisher Helios G4 FIB/SEM microscope. The top-view and cross-sectional SEM morphological studies were performed at 2 keV collecting emitted secondary electrons. Before obtaining the cross-section images, a protective platinum layer was deposited on both alloys to protect the lithium-based conversion layer surface from gallium damage during FIB milling. Besides, the grain boundaries of the aluminum alloys are very sensitive to gallium ions exposure during FIB milling [43]. This sensitivity is attributed to the fact that aluminum alloys have a higher cohesive energy compared to gallium leading to gallium segregation on the aluminum surface in order to decrease the grain boundary energy of the aluminum alloy [44]. Focused ion beam sectioning was conducted in blind-mode where the ion beam was used for milling. In this way the deposited platinum layer can be omitted.

2.2.4. Raman spectroscopy

Raman spectroscopy has been performed with a LabRAM HR Evolution instrument (HORIBA Scientific) equipped with a confocal microscope (objective 100x) and a solid-state laser of 532 nm (max. 1 mW). Prior to the analysis, metal coupons of 1 cm^2 for both AA2024-T3 and AA2198-T8 were immersed for 30 min in freshly prepared 10^{-1} M aqueous NaCl electrolyte in the presence and absence of 10^{-2} M Li_2CO_3 buffered at pH 10. Following immersion, the metal samples were dried under flowing nitrogen gas.

3. Results

3.1. Potentiodynamic polarization measurements

Fig. 1 shows typical OCP curves measured at pH 10 for AA2024-T3 and AA2198-T8 in the absence and presence of lithium carbonate. In both cases, OCP stabilization is shown and no rapid OCP changes are observed that would otherwise impair the thereafter polarization measurements. OCP curves are obtained for the whole selected pH range and the according graphs are given as supplementary information (Figure S1).

With regards to Fig. 1, in the absence of lithium carbonate, it is observed that AA2024-T3 presents a relatively constant potential under OCP conditions however a different behaviour is seen for AA2198-T8. For the aluminum-lithium alloy a drop in the potential of approximately 0.05 V is observed within the first minutes of immersion in the electrolyte after which the potential recovers to more positive values and remains stable. In the presence of lithium carbonate, the potential of both alloys is negatively shifted compared to the potential they adopt in the absence of lithium carbonate. Furthermore, within the first minutes of immersion in the lithium carbonate containing electrolyte a sharp drop in the potential is observed for both AA2024-T3 and AA2198-T8. Following this sharp drop, the potential is increasing to more noble values and adopts a steady state. It should be noted that this behaviour is only observed at pH 10 and further discussion is provided in the following sections.

Potentiodynamic polarization measurements were performed in 10^{-1} M chloride-containing aqueous bulk electrolyte at systematically varied pH both in the absence and presence of 10^{-2} M Li_2CO_3 in order to investigate the corrosion protection offered in the presence of lithium carbonate as a function of the bulk electrolyte pH. Fig. 2 and Fig. 3 show the typical potentiodynamic curves for AA2024-T3 and AA2198-T8 and the derived electrochemical parameters for each alloy are summarized in Table 3 and Table 4 accordingly.

By comparing Fig. 2 with Fig. 3, it is observed that lithium carbonate does not demonstrate effective corrosion inhibition when the pH of the bulk electrolyte is adjusted between pH 2 and pH 7 for both the AA2024-T3 (Fig. 2a-c) and AA2198-T8 alloy (Fig. 3a-c). Additionally, the AA2024-T3 alloy demonstrates nobler OCP values than AA2198-T8 between pH 2 and pH 7 as observed by Table 3 and Table 4 accordingly. With respect to the AA2024-T3 alloy, at pH 2 both in the absence (black curve) and presence (red curve) of lithium carbonate the cathodic branch shows a diffusion-limited behavior between − 0.68 V vs SHE and − 0.92 V vs SHE and the absence of passivation in the anodic branch indicates immediate pitting under polarization conditions (Fig. 2a). At pH 4, the cathodic branch of the polarization curves shifts to lower current densities indicating slower kinetics on the cathodic reactions (Fig. 2b). In the absence of lithium carbonate, a diffusion-limited behavior is observed between − 0.57 V vs SHE and − 0.92 V vs SHE, however a diffusion-limited region is not distinctly seen in the presence of lithium carbonate whilst the corresponding cathodic current densities remain higher compared to the blank solution (Fig. 2b). Still, the absence of a passivation region in the anodic branch indicates immediate pitting corrosion both in the absence and presence of lithium

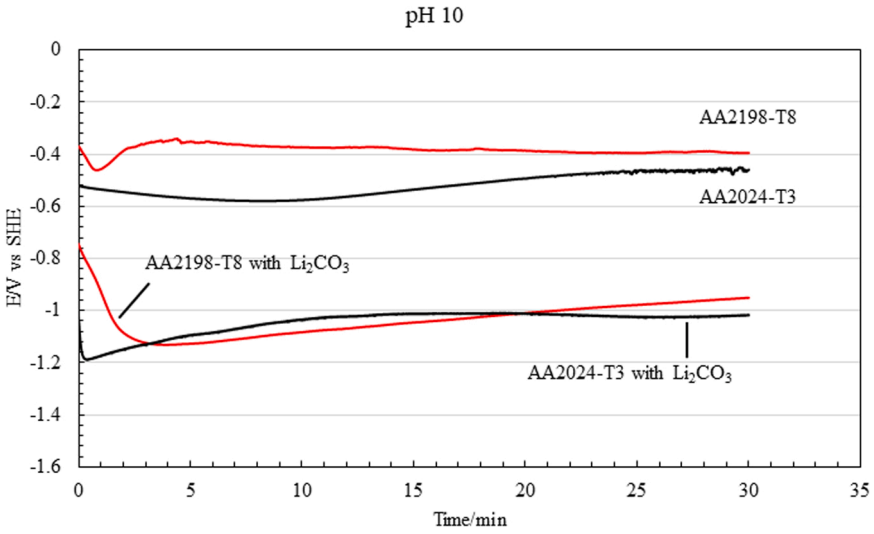

Fig. 1. Typical open circuit potential of AA2024-T3 and AA2198-T8 at pH 10 in 10^{-1} M NaCl in the absence and presence of Li_2CO_3.

carbonate in the bulk electrolyte under polarization conditions (Fig. 2b). At near-neutral pH, the polarization curves both in the absence and presence of lithium carbonate present a similar behavior. In both cases, the AA2024-T3 alloy instantly undergoes pitting corrosion under anodic polarization conditions and a diffusion-limited behavior is observed between − 0.68 V vs SHE and − 0.92 V vs SHE (Fig. 2c).

Likewise, at pH 2 the AA2198-T8 alloy undergoes immediate pitting corrosion under anodic polarization conditions both in the absence and presence of lithium carbonate (Fig. 3a). A diffusion-limited behavior is also observed in the cathodic branch of the polarization curve however in the presence of lithium carbonate the cathodic branch shifts to lower current densities (Fig. 3a red curve). Accordingly, at pH 4 immediate pitting corrosion is also seen both in the absence and presence of lithium carbonate along with a diffusion-limited behavior in the cathodic branch ranging from −0.5 V to −0.9 V vs SHE for the blank solution. For the lithium salt solution, a significantly smaller diffusion-limited region of − 0.5 V to − 0.7 V vs SHE was observed (Fig. 3b). Contrary to AA2024-T3, a different response is obtained for AA2198-T8 in the presence of lithium carbonate in that the cathodic branch shifts to lower cathodic densities compared to the corresponding blank solution (Fig. 3c) thus limiting the corrosion current density to lower values (Table 4) [45].

Under moderately alkaline conditions at pH 10 and in the absence of lithium carbonate from the bulk electrolyte a pitting potential is observed for AA2024-T3 at − 0.32 V vs SHE along with a diffusion-limited behavior between − 0.64 V vs SHE and − 0.80 V vs SHE (Fig. 2d black curve). Contrary, in the presence of lithium carbonate in the bulk electrolyte the OCP shifts to less noble potentials by approximately 0.5 V to − 0.95 V vs SHE and both the anodic and cathodic branch shift to higher current densities by two orders of magnitude indicating higher oxidation and reduction kinetics, respectively (Fig. 2d red curve, Table 3). The increase of i_{corr} in the presence of lithium carbonate by approximately two orders of magnitude as compared to the reference measurement at pH 10 is also suggesting faster anodic dissolution kinetics (Table 3). However, a distinct passive region of 0.81 V is observed in the anodic branch in the presence of the inhibitor with the breakdown potential to be recorded at − 0.16 V vs SHE. Similarly, the AA2198-T8 alloy demonstrates a pitting potential at − 0.19 V vs SHE under anodic polarization conditions (Fig. 3d) which is more noble than the one observed for AA2024-T3 in the absence of the inhibitor (Fig. 2d). In the cathodic branch a relative diffusion-limited behavior between 0.61 V vs SHE and − 1.03 V vs SHE is also observed (Fig. 3d black curve). However, in the presence of lithium carbonate the OCP value of the AA2198-T8 alloy shifts to less noble potentials to about − 0.92 V vs SHE and a passive range of approximately 1.02 V is distinctly seen in the anodic branch (Fig. 3d red curve) which is larger than the one observed for AA2024-T3 alloy (Fig. 2d). Additionally, both the anodic and cathodic branch shift to higher current densities when lithium carbonate is present in the bulk electrolyte by one order of magnitude also indicating faster kinetics (Table 4). Interestingly, however, in the presence of lithium carbonate the i_{corr} value obtained for AA2198-T8 (Table 4) is an order of magnitude lower compared to that for AA2024-T3 (Table 3).

Lastly, at strongly alkaline conditions of pH 13 the polarization curves of AA2024-T3 recorded both in the absence and presence of lithium carbonate present a similar electrochemical behavior except the fact that in the presence of lithium carbonate the anodic branch shifts to lower current densities in contrast to the cathodic branch which shifts to higher cathodic densities (Fig. 2e). In both cases, the OCP value is close to − 1.15 V vs SHE and a pseudo-passive region is observed to initiate at − 0.91 V vs OCP. Likewise, the AA2198-T8 alloy also exhibits a pseudo-passive behavior initiating at − 0.89 V vs SHE but in the presence of lithium carbonate the anodic branch shifts to lower current densities indicating slower anodic kinetics (Fig. 3e). Still, the i_{corr} obtained for both AA2024-T3 and AA2198-T8 is higher by approximately three orders of magnitude compared to the values obtained for the other selected pH ranges. This is attributed to the fact that aluminum is thermodynamically unstable under strongly alkaline conditions leading to the anodic dissolution of aluminum generating $Al(OH)_4^-$ ions [46].

3.2. *In-situ optical time-lapse microscopy*

The polarization experiments described above give no information on the location, size or shape of the corrosion features occurring on the surface of the exposed aluminum alloys or how these are influenced by the addition of lithium carbonate. With the aim of determining the localization of corrosion related reactions in the presence and absence of lithium carbonate, a series of experiments were performed in which the corroding aluminum surface of both AA2024-T3 and AA2198-T8 was observed using in-situ time-lapse microscopy. Optical microscopy cannot quantify the rate of electrochemical processes however it does permit a precise localization of the corrosion features and quantification of their lateral propagation.

Fig. 4 and Fig. 5 display a series of images taken ex-situ at the end of the in-situ time lapse microscopy for AA2024-T3 and AA2198-T8 respectively. For both alloys the exposed metal surface was immersed in 10^{-1} M NaCl for 24 h in the presence and absence of lithium carbonate and the pH of the electrolyte varied at the selected range, i.e. pH 2 to pH 13. The exposed aluminum area is a circular region of 0.196 mm^2 and PTFE tape is seen at the periphery. In all cases the total

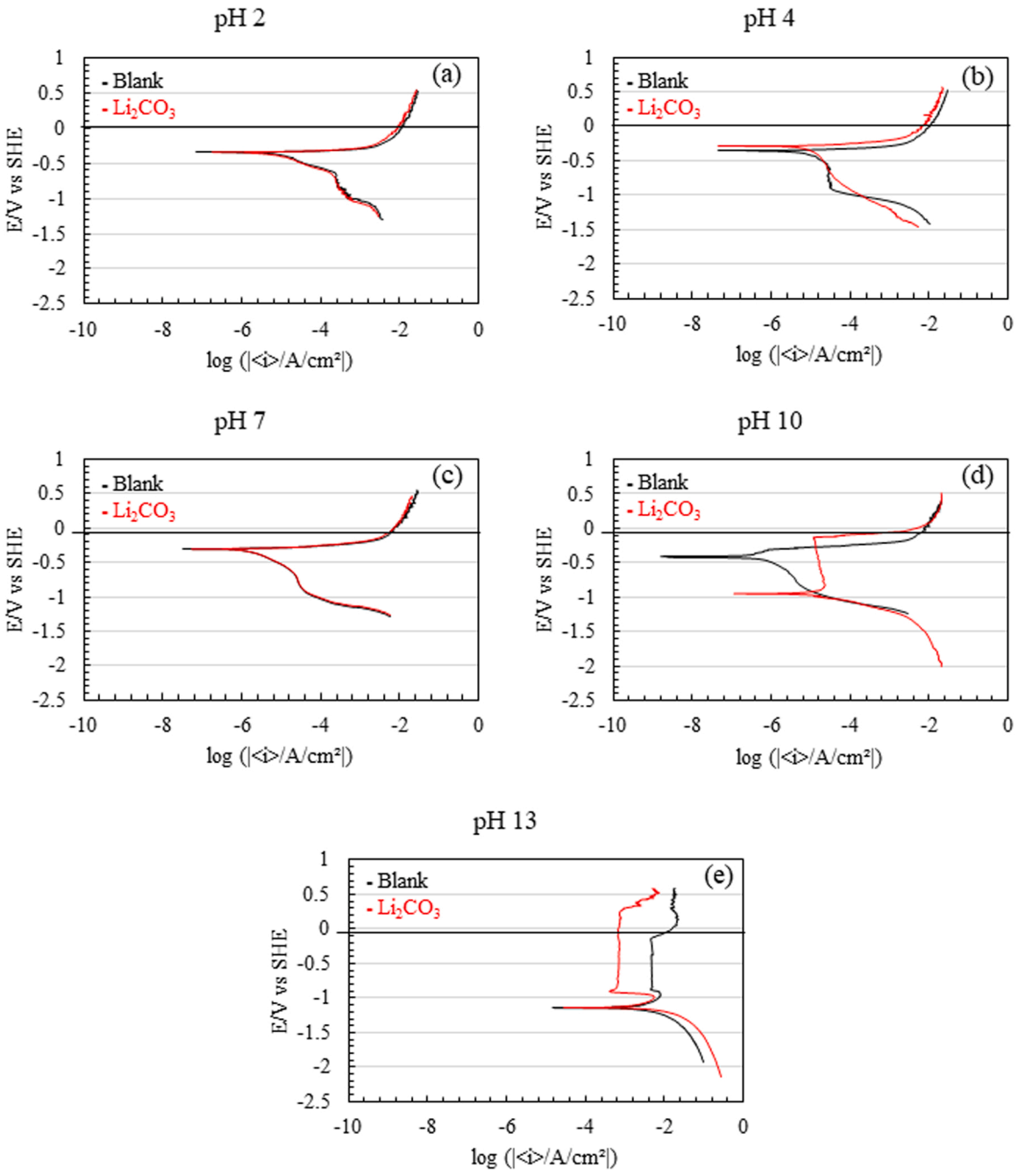

Fig. 2. Typical potentiodynamic polarization curves as a function of time of bare AA2024-T3 exposed in 10^{-1} M aqueous NaCl electrolyte at systematically varied pH. The black curves indicate the absence and the red curves indicate the presence of 10^{-2} M Li_2CO_3 within the electrolyte. Label key: (a) pH 2, (b) pH 4, (c) pH 7, (d) pH 10, and (e) pH 13.

area of corrosion developed during the immersion time and at the different pH environments is optically seen as either dark local spots or dark regions against the lighter metal background. The corresponding videos for each in-situ time-lapse experiment are provided as supplementary information (S2).

In most cases, during in-situ time-lapse microscopy hydrogen evolved from the surface of the bare metal that eventually minimized the legibility of the optical images taken during the experimental time. Therefore, it was not possible to record the lateral corrosion propagation as a function of time. Instead, the ex-situ images taken immediately following the experiment and displayed in Fig. 4 and Fig. 5 were analyzed and the total corrosion area was measured. During image analysis, the dark local spots or dark regions developed against the lighter metal background were considered as corrosion during the analysis of the corroded area.

The total corrosion area is displayed as a function of pH in the presence and absence of Li_2CO_3 in Fig. 6 for AA2198-T8 (Fig. 6a) and AA2024-T3 (Fig. 6b). For both alloys, between pH 2 and pH 7 there is a small reduction in the corrosion area on the alloy surface in the presence of lithium carbonate which is 24% for pH 2 and 10–16% for pH 4 and pH 7. Greater reduction in the corrosion area is observed at pH 10 which corresponds to approximately 68% for AA2024-T3 and 78% for AA2198-T8. Lastly, no significant change was observed in the corrosion area of both aluminum alloys in the presence of lithium carbonate at pH 13 and in both cases the metal surface was heavily corroded (Fig. 4j and Fig. 5j).

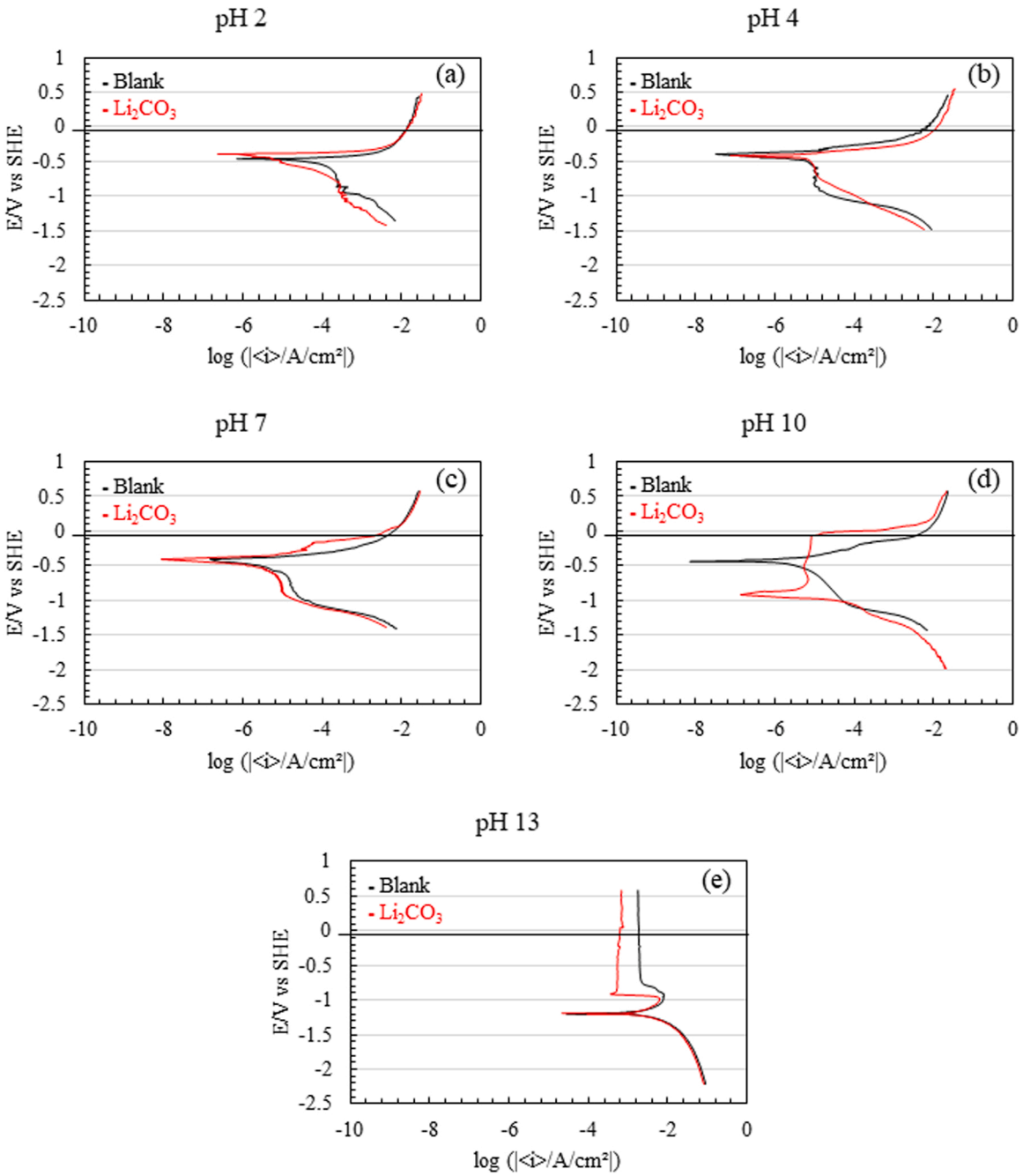

Fig. 3. Typical potentiodynamic polarization curves as a function of time of bare AA2198-T8 exposed in 10^{-1} M aqueous NaCl electrolyte at systematically varied pH. The black curves indicate the absence and the red curves indicate the presence of 10^{-2} M Li_2CO_3 within the electrolyte. Label key: (a) pH 2, (b) pH 4, (c) pH 7, (d) pH 10, and (e) pH 13.

With respect to the polarization curves shown in Fig. 2 and Fig. 3, lithium carbonate demonstrates effective corrosion protection under moderately alkaline conditions at pH 10 for both AA2024-T3 and AA2198-T8. This protective behavior of lithium carbonate is also optically observed during the in-situ time-lapse microscopy as made manifest by the great corrosion area reduction for both aluminum alloys (Fig. 6). Therefore, it is important to further investigate the surface features developed as a function of time under such conditions for both AA2024-T3 and AA2198-T8. Fig. 7 and Fig. 8 display sequential optical images taken in-situ at pH 10 showing corrosion initiation and propagation for exposed AA2024-T3 and AA2198-T8 alloy accordingly both in the absence and presence of 10^{-2} M Li_2CO_3.

In the absence of lithium carbonate, pitting corrosion initiates within the first minute of immersion on the exposed surface of AA2024-T3 in the form of dark local points against the lighter uncorroded background (Fig. 7b) [47]. At the pitting sites metal oxidation occurs and the aluminum aquo-cations move into the interfacial region creating a charge imbalance which is neutralized by the ingress flow of chloride and hydroxyl ions promoting further corrosion processes [48]. Promotion of pitting corrosion on AA2024-T3 in the absence of lithium carbonate is visible through Fig. 7c-e in which a dense population of local dark pitting sites is observed against the lighter uncorroded background and the lateral corroded area around the local anodes is covering approximately 56% of the total exposed metal surface following 24 h of immersion to the bulk electrolyte.

In the presence of lithium carbonate, pitting corrosion also initiates

Table 3
Electrochemical parameters for AA2024-T3 as obtained from the potentiodynamic curves displayed in Fig. 2.

pH	Reference		10^{-2} M Li_2CO_3	
	E_{corr} (V_{SHE})	i_{corr} ($A.cm^{-2}$)	E_{corr} (V_{SHE})	i_{corr} ($A.cm^{-2}$)
2	-0.295	7.23×10^{-6}	-0.297	6.07×10^{-6}
	$\pm$ 0.005	$\pm$ 0.24 $\times 10^{-6}$	$\pm$ 0.002	$\pm$ 0.19 $\times 10^{-6}$
4	-0.297	1.05×10^{-6}	-0.292	1.21×10^{-6}
	$\pm$ 0.001	$\pm$ 0.41 $\times 10^{-6}$	$\pm$ 0.006	$\pm$ 0.60 $\times 10^{-6}$
7	-0.273	1.05×10^{-6}	-0.277	9.94×10^{-7}
	$\pm$ 0.009	$\pm$ 3.67 $\times 10^{-6}$	$\pm$ 0.003	$\pm$ 1.57 $\times 10^{-7}$
10	-0.457	1.61×10^{-7}	-0.957	1.36×10^{-5}
	$\pm$ 0.015	$\pm$ 0.23 $\times 10^{-7}$	$\pm$ 0.031	$\pm$ 0.03 $\times 10^{-5}$
13	-1.159	1.45×10^{-3}	-1.153	1.27×10^{-3}
	$\pm$ 0.007	$\pm$ 0.21 $\times 10^{-3}$	$\pm$ 0.009	$\pm$ 0.14 $\times 10^{-3}$

Table 4
Electrochemical parameters for AA2198-T8 as obtained from the potentiodynamic curves displayed in Fig. 3.

pH	Reference		10^{-2} M Li_2CO_3	
	E_{corr} (V_{SHE})	i_{corr} ($A.cm^{-2}$)	E_{corr} (V_{SHE})	i_{corr} ($A.cm^{-2}$)
2	-0.408	4.87×10^{-6}	-0.408	7.72×10^{-6}
	$\pm$ 0.007	$\pm$ 0.38 $\times 10^{-6}$	$\pm$ 0.003	$\pm$ 1.12 $\times 10^{-6}$
4	-0.350	1.94×10^{-6}	-0.377	1.21×10^{-6}
	$\pm$ 0.031	$\pm$ 0.23 $\times 10^{-6}$	$\pm$ 0.009	$\pm$ 0.62 $\times 10^{-6}$
7	-0.390	3.05×10^{-6}	-0.364	4.96×10^{-7}
	$\pm$ 0.004	$\pm$ 0.78 $\times 10^{-6}$	$\pm$ 0.006	$\pm$ 2.41 $\times 10^{-7}$
10	-0.416	9.52×10^{-7}	-0.913	3.42×10^{-6}
	$\pm$ 0.016	$\pm$ 4.03 $\times 10^{-7}$	$\pm$ 0.002	$\pm$ 0.23 $\times 10^{-6}$
13	-1.222	1.49×10^{-3}	-1.220	1.02×10^{-3}
	$\pm$ 0.002	$\pm$ 0.06 $\times 10^{-3}$	$\pm$ 0.002	$\pm$ 0.04 $\times 10^{-3}$

within the first minute of immersion to the bulk electrolyte on the exposed AA2024-T3 surface and appears as local dark points against the lighter uncorroded background (Fig. 7g). Over the total experimental time a dense population of clusters of pits is observed across the exposed aluminum surface (Fig. 7h-j) however the lateral corroded area around the local anodes after 24 h of immersion is reduced and covers approximately 15% of the total exposed aluminum surface (Fig. 7j). Please note that it is not possible to determine the depth of the pitting sites due to resolution of the optical microscopy.

When bare AA2198-T8 is exposed to the bulk electrolyte in the absence of lithium carbonate, hydrogen evolution is immediately observed nucleating close to the metal/tape interface and local breakdown events of the passive natural oxide film are seen as dark local points against the lighter alloy matrix (Fig. 8b). The visualization of hydrogen evolution in the case of AA2198-T8 as opposed to AA2024-T3 may suggest faster corrosion kinetic phenomena. Following 10 min of immersion, in the absence of lithium carbonate the bare AA2198-T8 surface still does not show significant changes (Fig. 8c) whilst hydrogen bubbles increase in size. Contrary, in the presence of lithium carbonate the lighter metallic background seen in Fig. 8g becomes rather uniformly darker after 10 min of immersion (Fig. 8h). This darkening of the metallic background becomes more evident for longer immersion times as seen in Fig. 8i. Pitting corrosion proceeds vigorously at the exposed area of AA2198-T8 in the absence of lithium carbonate as observed by the dense population of pitting sites evolved following 218 min of immersion (Fig. 8d). In addition, the thickening of the corrosion products at the top-surface of the alloy leads to reduced legibility of the image (Fig. 8d) and a heavily attacked surface is observed after 24 h of exposure to chloride-containing electrolyte (Fig. 8e). The lateral corroded area around the local anodes after 24 h of immersion for AA2198-T8 is covering approximately 85% of the total exposed metal surface which is slightly larger compared to the value obtained for AA2024-T3.

In the presence of lithium carbonate, at immediate exposure of the AA2198-T8 alloy to the aqueous chloride electrolyte excess hydrogen evolution is observed close to the edges of the masking tape (Fig. 8g). Within 10 min of immersion, visual indications of a layer formation are observed on the exposed alloy surface which follows the local topography as determined during polishing while occurrence of pitting seems to be significantly reduced (Fig. 8h). Following 218 min of immersion, the presence of the formed layer becomes more evident due to the darkening of this feature as a function of time and no further hydrogen evolution is observed (Fig. 8i) and this feature preserves its integrity even after 24 h of total experimental time (Fig. 8j). The lateral corroded area around the local anodes after 24 h of immersion for AA2198-T8 is reduced covering approximately 15% of the total exposed metal surface.

3.3. Surface Characterization

SEM images were acquired from AA2024-T3 and AA2198-T8 corroded in the presence of lithium carbonate at pH 10 with the aim to characterize the morphology of corrosive attack and the layer formed on the surface of exposed aluminum as observed during the in-situ time-lapse experiments above. The surface characterization was focused on pH 10 as according to the polarization curves shown in Fig. 2 for AA2024-T3 and Fig. 3 for AA2198-T8 a passive region in the anodic part of the curve is only observed under pH 10 and at the same time a significant corrosion area reduction for both aluminum alloys is only

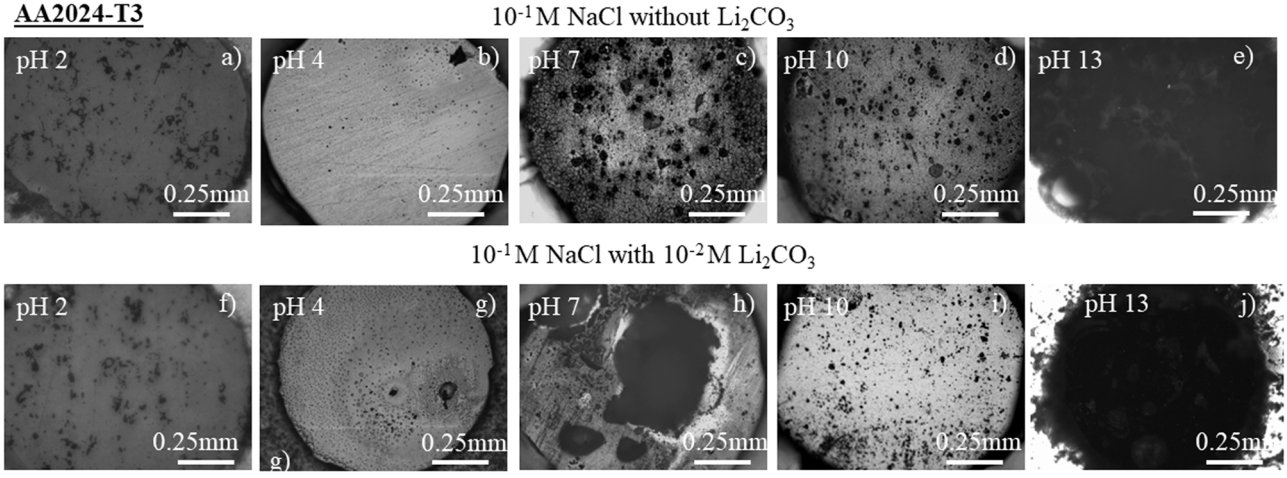

Fig. 4. Optical images of bare AA2024-T3 taken ex-situ. The exposed metal surface was immersed for 24 h in 10^{-1} M NaCl at varied pH from 2 to 13 in the absence (a-e) and presence (f-j) of 10^{-2} M Li_2CO_3. The photos illustrate the total corrosion area developed at the end of in-situ time-lapse microscopy.

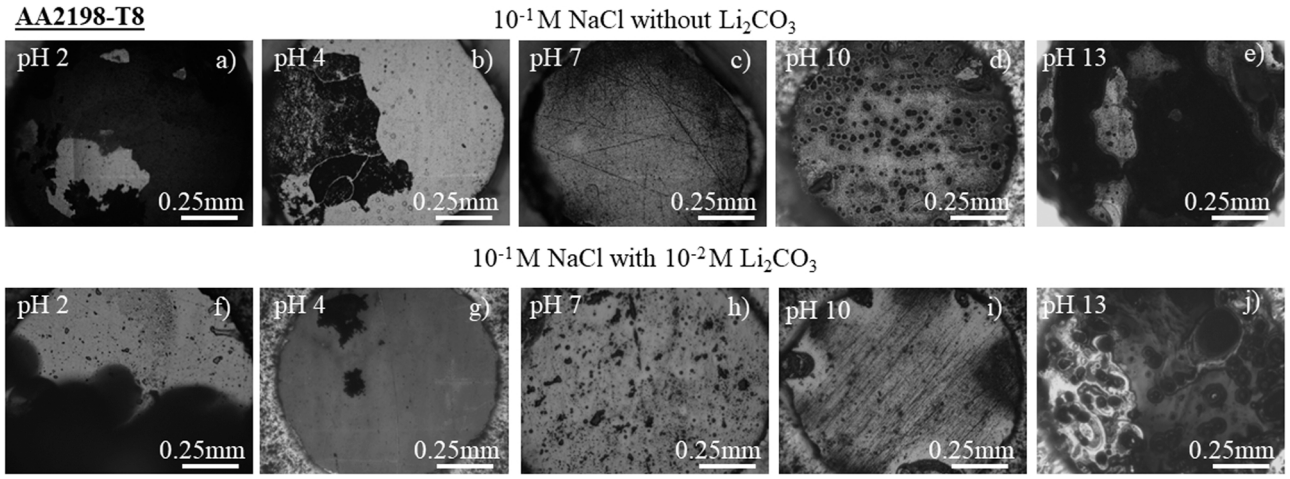

Fig. 5. Optical images of bare AA2198-T8 taken ex-situ. The exposed metal surface was immersed for 24 h in 10^{-1} M NaCl at varied pH from 2 to 13 in the absence (a-e) and presence (f-j) of 10^{-2} M Li_2CO_3. The photos illustrate the total corrosion area developed at the end of in-situ time-lapse microscopy.

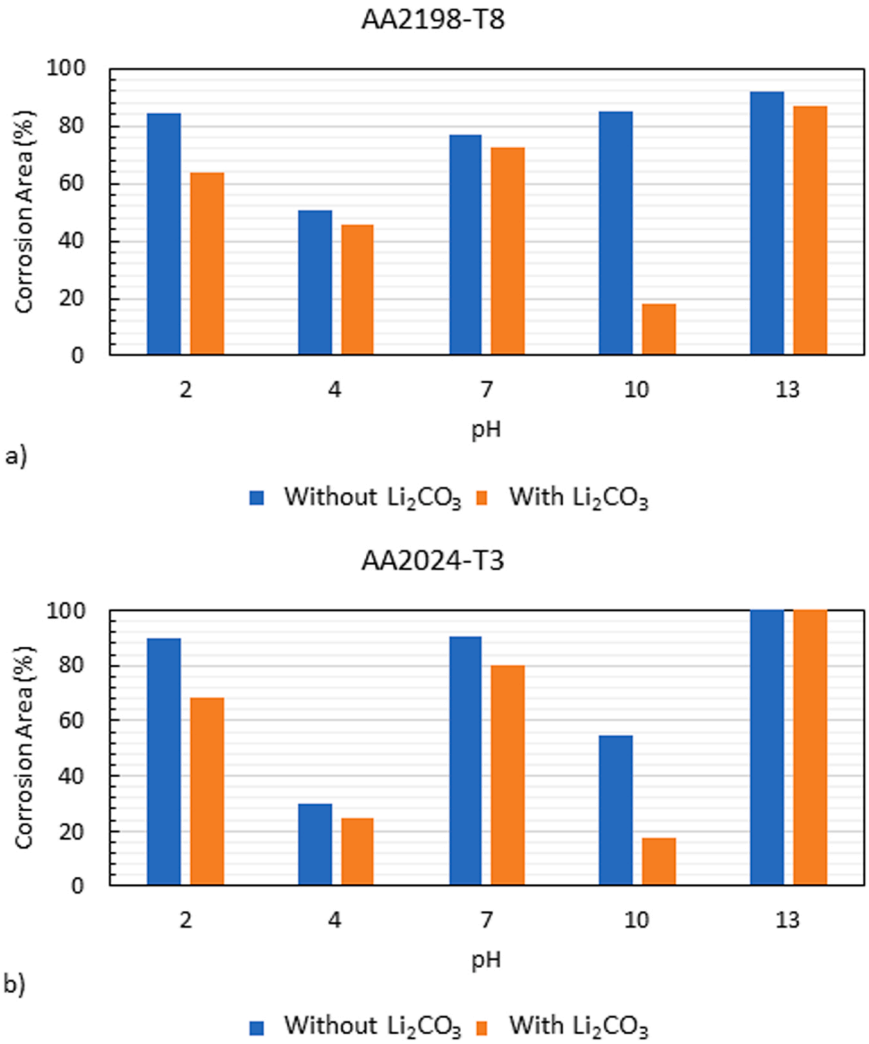

Fig. 6. Corrosion area expressed as percentage of the total exposed metal surface for AA2198-T8 (a) and AA2024-T3 (b) as a function of pH in the presence and absence of 10^{-2} M Li_2CO_3. The area is recorded by image analysis of the photos displayed in Fig. 4 and Fig. 5.

observed at pH 10 during in-situ time-lapse microscopy. As such, Fig. 9 shows a series of secondary SEM images obtained from the top-surface and cross-section of AA2024-T3 (Fig. 9a-b) and AA2198-T8 (Fig. 9c-d) following 30 min of immersion in aqueous 10^{-1} M chloride electrolyte at pH 10 containing 10^{-2} M Li_2CO_3. The 30 min of immersion to the corrosive medium was selected based on the time both alloys are

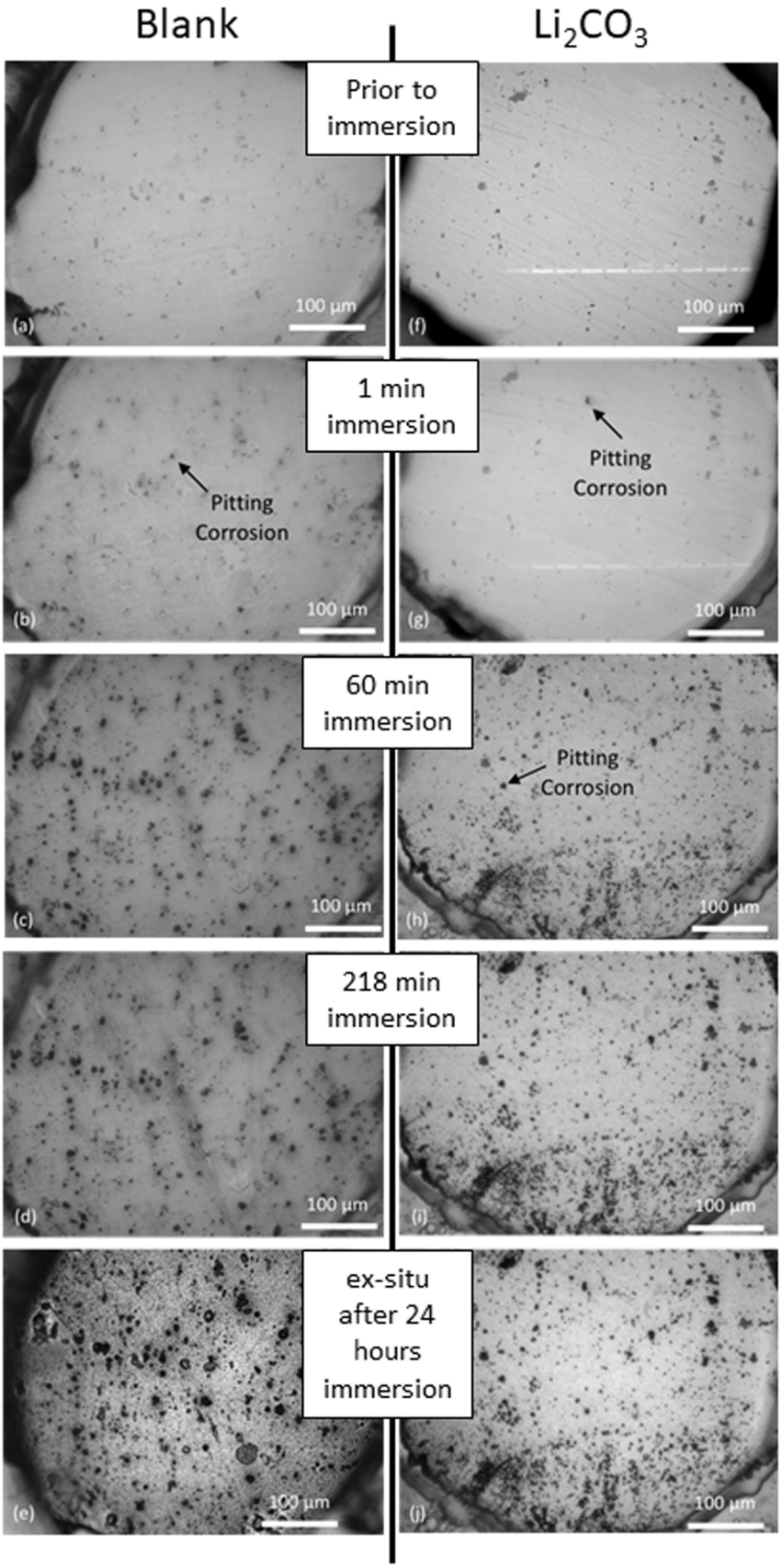

Fig. 7. Optical images taken during in-situ time-lapse microscopy. The photos illustrate the progression of corrosion on the bare AA2024-T3 surface under immersion conditions in 10^{-1} M NaCl at pH 10 in the absence (a-e) and presence (f-j) of 10^{-2} M Li_2CO_3. Time key following immersion to electrolyte: (a & f) prior exposure, (b & g) 1 min, (c & h) 60 min, (d & i) 218 min, and (e & j) ex-situ image after 24 h.

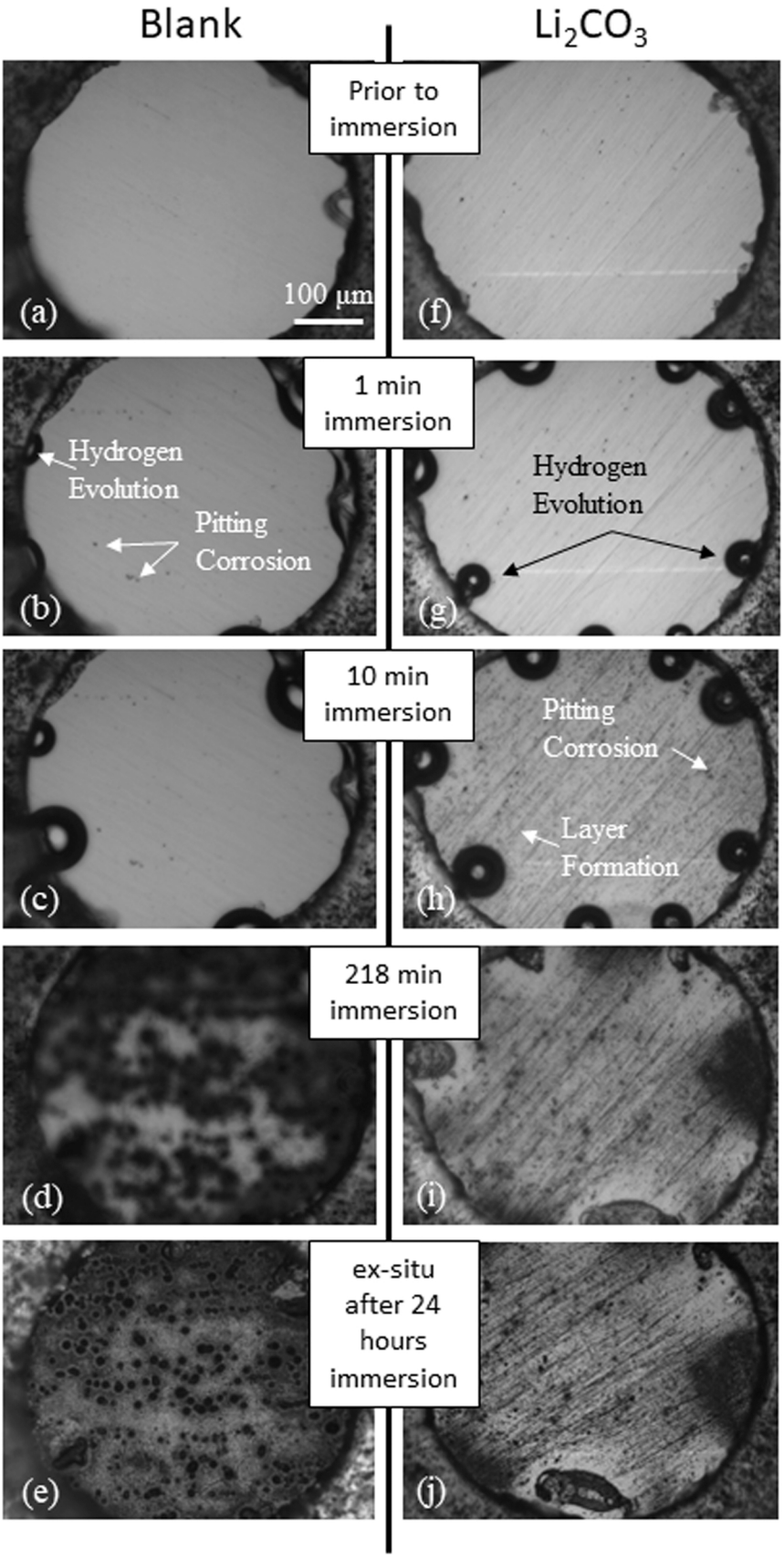

Fig. 8. Optical images taken during in-situ time-lapse microscopy. The photos illustrate the progression of corrosion on the bare AA2198-T8 surface under immersion conditions in 10^{-1} M NaCl at pH 10 in the absence (a-e) and presence (f-j) of 10^{-2} M Li_2CO_3. Time key following immersion to electrolyte: (a & f) prior exposure, (b & g) 1 min, (c & h) 60 min and 10 min accordingly, (d & i) 218 min, and (e & j) ex-situ image after 24 h.

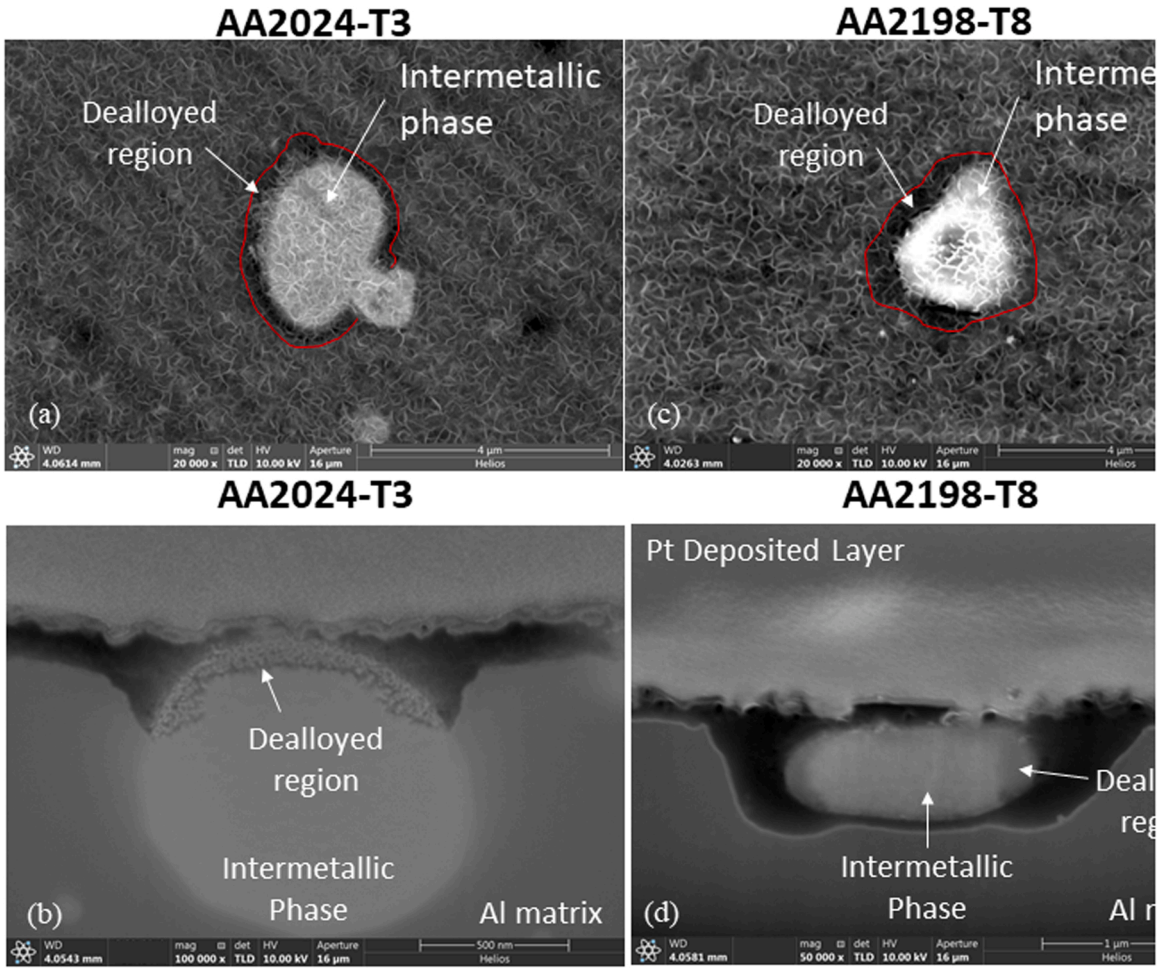

Fig. 9. Secondary SEM images of both AA2024-T3 and AA2198-T8 following 30 min of immersion in 10^{-1} M aqueous NaCl electrolyte containing 10^{-2} M Li_2CO_3 buffered at pH 10. Label key: (a) top-surface and (b) cross-section of AA2024-T3 alloy and (c) top-surface and (d) cross-section of AA2198-T8 alloy. Electron beam to specimen stage angle is 52°.

immersed in the bulk solution under OCP conditions prior to the polarization experiments.

Fig. 9a and c show the typical top-surface secondary image of AA2024-T3 and AA2198-T8 respectively taken over a secondary intermetallic phase particle (S-phase) [49,50] which appear lighter against the darker background. For both aluminum alloys the top-surface is covered by a homogeneous randomly oriented fine-flake morphology which is characteristic for hydrated aluminum oxides [48,49,51]. The S-phase boundary, which is defined on the image by the red curve, appears darker compared to the rest of the surface however it is not possible to identify the origin of this feature based solely on the top surface image and therefore secondary cross-sectional SEM images were taken (Fig. 9b and d).

Fig. 9b and d show cross-sectional secondary SEM images taken along the S-phase on AA2024-T3 and AA2198-T8 respectively on which the platinum deposited layer appears bright in both top-view SEM images. In both cases the intermetallic particle appears lighter against the darker aluminum background and for AA2024-T3 a porous structure is observed in the top side region of the particle which is identified as the dealloyed area leaving a Cu-rich remnant (Fig. 9b) [47,50,52,53]. Indications of intermetallic particle dealloying are also visible in the case of AA2198-T8 appearing as dark grey regions along the edges of the particle (Fig. 9d). As described above, following the intermetallic particle dealloying and trenching initiation, local dissolution proceeds to the alloy matrix/particle interphase seen as a dark region around the particle on both AA2024-T3 (Fig. 9b) and AA2198-T8 (Fig. 9d) [47,50,53,54]. Notable is the observation that in the case of AA2198-T8 the dissolution at the alloy matrix/particle interphase runs along the periphery of the intermetallic particle possibly indicating particle undercutting from the aluminum matrix (Fig. 9d). The highest susceptibility of AA2198-T8 compared to AA2024-T3 has also been reported elsewhere [55] and it is proposed that this behaviour is associated with the presence of the T1 (Al_2CuLi) phase [33–36,56–58]. The characteristic features of hydrated aluminum oxides seen at the top-surface secondary images of both aluminum alloys are not seen at the cross-sectional secondary images taken at the intermetallic phase. Instead, a dark area is visualized suggesting trench formation. However, it should be considered that lithium is a light element of very low energy of characteristic radiation (54 eV) and therefore it is very difficult to analyze using conventional detectors [59,60]. In addition, previous work has indicated that an aluminum-lithium conversion layer even forms within trenched regions using TEM [49]. Consequently, Raman spectroscopy measurements were performed in order to provide the chemical structure by which the protective layer formed on AA2024-T3 and AA2198-T8 can be identified.

Fig. 10 shows a series of Raman spectra obtained from AA2024-T3 and AA2198-T8 following 30 min of immersion in aqueous 10^{-1} M chloride electrolyte at pH 10 in the presence and absence of 10^{-2} M Li_2CO_3. The characteristic bands for the different forms of aluminum (hydr)oxides are mainly observed in the low-wavenumber region between 200 and 1200 cm^{-1} which comprise of the δ(OH) and γ(OH) modes related to the Al(OH) deformation and Al-O-Al skeletal stretching

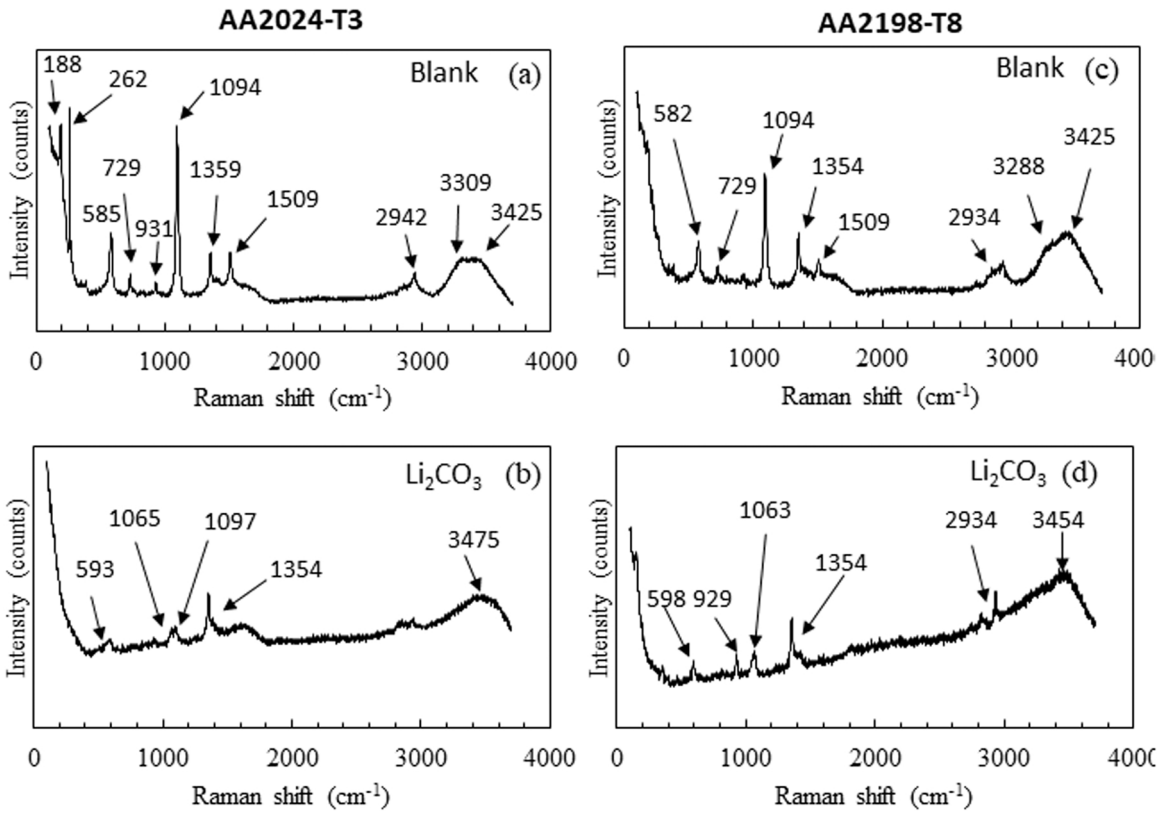

Fig. 10. Typical Raman spectroscopy obtained after 30 min of immersion in 10^{-1} M aqueous NaCl electrolyte for AA2024-T3 (a, b) and AA2198-T8 (c, d) in the absence and presence of 10^{-2} M Li_2CO_3 at pH 10 accordingly.

vibrations [18,61,62]. The 585 cm^{-1} and 582 cm^{-1} bands observed in the absence of the inhibitor for AA2024-T3 (Fig. 10a) and AA2198-T8 (Fig. 10c) respectively have been identified as non-solvated aluminate [62]. However, in the presence of lithium carbonate the aluminate bands shift to 593 cm^{-1} and 598 cm^{-1} for AA2024-T3 (Fig. 10b) and AA2198-T8 respectively (Fig. 10d) which is attributed to the solvation of aluminate ions to coordinated water numbers ≥ 4 [62]. It is also proposed that the incorporation of water molecules via the formation of hydrogen bonds can decrease the enthalpy of the amorphous aluminate clusters thus leading to a more stable structure [62]. The hydroxyl stretching region is mainly observed between 2800 and 3700 cm^{-1} and is characteristic of the ν(OH) stretching mode [61]. The Raman bands identified for gibbsite, bayerite, diaspore and boehmite are greatly overlapping [61] therefore it is difficult to distinguish the identity of the aluminum (hydr)oxide type from the Raman spectra given in Fig. 10. However, under alkaline conditions bayerite is considered to be the stable form of the aluminum trihydroxide [17]. Lastly, in the presence of lithium carbonate a new Raman band is present at 1065 cm^{-1} and 1063 cm^{-1} for AA2024-T3 (Fig. 10b) and AA2198-T8 (Fig. 10d) respectively which has been identified elsewhere as $Li_2Al_4CO_3(OH)_{12}{\cdot}3\,H_2O$ layered double hydroxide (Al-Li LDH) [18].

4. Discussion

The OCP measurements taken prior to potentiodynamic polarization reveal no rapid OCP changes however notable differences in the OCP curves are observed at pH 10. In the absence of lithium carbonate a potential drop is observed for AA2198-T8 within the first minutes of immersion in the electrolyte. A similar OCP behaviour for aluminum-lithium alloys is reported in literature which is attributed to the dissolution of the natural air-formed aluminum oxide in response to the presence of lithium in the alloy matrix [17,33,34,63]. In the presence of lithium carbonate, the potential adopted by both AA2024-T3 and AA2198-T8 is shifted to less noble values and a sharp potential drop is observed within the first minutes of immersion after which the potential recovers to more noble values followed by a plateau. This is a typical OCP behaviour reported for aluminum alloys in the presence of lithium salts [6,49]. The initial sharp drop in the potential is attributed to the dissolution of air-formed oxide layer and s-phase dealloying as also observed during the SEM characterization of both aluminum alloys in Fig. 9 [6,49]. As the potential increases into a steady state, the initial formation of the lithium containing protective layer is taking place and grows further [6]. The SEM images (Fig. 9) suggest that the lithium containing protective layer is fully formed after 30 min of immersion in lithium carbonate electrolyte for both AA2025-T3 and AA2198-T8.

The potentiodynamic polarization measurements obtained for AA2024-T3 (Fig. 2d) and AA2198-T8 (Fig. 3d) in aqueous chloride electrolyte in the presence of lithium carbonate at pH 10 suggest an active-to-passive transition that does not occur in the blank solution. Furthermore, under such alkaline condition, the presence of an AL-Li LDH layer is identified on the surface of both aluminum alloys through microscopic (Fig. 9) and Raman (Fig. 10b and d) characterization. With respect to the formation mechanism of the lithium containing layer on aluminum alloys, it is proposed by Visser et al. [6] and Kosari et al. [49] that it occurs in multiple stages. The initial stages are identified as the activation phase where the aluminum (hydr)oxide is being weakened and this oxidation process contributes to the increased current density observed in the polarization curve of both AA2024-T3 (Fig. 2d) and AA2198-T8 (Fig. 3d) in the presence of lithium carbonate.

As mentioned earlier, the presence of Cu rich particles in the aluminum matrix contribute to the electrocatalytic activity of the cathodic oxygen reduction reaction [38] promoting chloride-induced corrosion on AA2024-T3 [30–32] and AA2198-T8 [17,33–36]. The addition of Cu alloying elements leads to the formation of secondary phase intermetallic particles including Al_2CuMg (S-phase) which account for approximately 60% of the intermetallic particles present on

Al-Cu alloys' surface and matrix [64,65]. With respect to Cu-enriched intermetallic particles, it has been shown that local corrosion proceeds in four steps: dealloying-driven initiation, trench initiation, depth propagation and particle undercutting [49,50,53]. Initially, nano-pitting is formed as a consequence of the intermetallic particles dealloying in which the active elemental constituents dissolve away [50]. This initial dissolution leaves a high-surface-area porous Cu network [66] for which it is reported that Cu clusters detach and may redistribute contributing to Cu enrichment [47,50,53]. Such dissolution can be distinguished as a highly porous dealloyed region in the intermetallic phase investigated laterally with SEM for AA2024-T3 (Fig. 9b). Such a porous structure is not readily seen in the intermetallic particle of AA2198-T8, for which dealloying is visible as grey regions along the edges of the particle (Fig. 9d). This optical difference of the intermetallic dealloying possibly suggests different dissolution kinetics between the aluminum alloys [53]. This is further supported by the current density recorded for AA2024-T3 and AA2198-T8 at pH 10 in the presence of lithium carbonate which is 1.36 $\bullet 10^{-5}$ A.cm^{-2} (Tables 3) and 3.42$\bullet 10^{-6}$ A.cm^{-2} (Table 4) respectively and differs by approximately an order of magnitude. The redistribution of Cu can lead to establishment of nano-galvanic coupling thus enhancing the driving force for local breakdown at the adjacent aluminum matrix. Local dissolution increases as a function of time and proceeds by discontinuous trenching at the alloy matrix and at the alloy matrix/metal interface closest to the dealloyed region. Such dissolution is optically observed as a dark region at the periphery of the intermetallic phase on the top-view SEM images in Fig. 9 for both AA2024-T3 and AA2198-T8. As corrosion proceeds, Cu may also undergo anodic dissolution within the corroding intermetallic particle which is attributed to the physical or electrical isolation of some copper segments [50,53]. At prolonged exposure time, the alloy matrix surrounding the particle is fully dissolved at which instance the intermetallic particle adopts its own corrosion potential leading to complete dealloying.

In the work of Kosari et al. [49,50,53] it is reported that the dark periphery of the intermetallic particle is indicative of slight trenching and selective element dissolution. Interesting is the fact that the formed lithium containing protective layer is able to cover the intermetallic phase on both AA2024-T3 and AA2198-T8 which would otherwise act as a preferential cathodic site if left exposed [47,49,51]. Kosari et al. [49] propose that the dissolution of the surrounding aluminum matrix results to local $Al(OH)_4^-$ saturation required for the formation of a conversion layer in the presence of lithium salts which contributes to slower dealloying of the intermetallic particle.

Under moderately alkaline conditions of pH > 9 anodic dissolution is promoted by both the presence of the aggressive chloride anions and the thermodynamic instability of the aluminum substrate which dissolves by reaction 2 for which the thermodynamic solubility product is $K_{sp} = 10^{-31.2}$ and $K_{sp} = 10^{-33.9}$ for amorphous aluminum (hydr)oxide and gibbsite, respectively, at 25 °C [46,67]. The equilibrium solubility of aluminum-based hydrolysis products as a function of pH also indicates that aluminate is the main form (reaction 3–5) in alkaline conditions and that the amorphous aluminum yields soluble concentrations significantly larger than the ones obtained from crystalline gibbsite [46,67]. It is proposed that moderate alkaline conditions lead to thicker aluminum hydroxide gel layers due to lower dissolution kinetic rate compared to strongly alkaline pH values [6]. The direct aluminum dissolution (reaction 3) is accompanied by hydrogen gas evolution produced through water reduction (reaction 2) [68,69].

$$2H_2O + 2e^- = H_2 + 2OH^- \quad (2)$$

$$Al = Al^{3+} + 3e^- \quad (3)$$

$$Al^{3+} + 3OH^- = Al(OH)_3 \quad (4)$$

$$Al(OH)_3 + OH^- = Al(OH)_4^- \quad (5)$$

Studies of the aluminate ion precipitation under moderately alkaline conditions indicated a precipitation sequence which increases according to the thermodynamic stability of the involved phases as amorphous → pseudo-boehmite → bayerite and is dictated by the pH and the concentration of aluminum ions [70,71]. Pseudo-boehmite is a partially hydrated boehmite where the excess of water leads to an irregular lattice extension and thus a less-ordered structured with a high specific surface (200–300 m^2/g) [71]. Consequently, the pseudo-boehmite surface favors the formation of bayerite via heterogeneous nucleation and this transformation is more dominant at high pH and aluminum concentration [70,71] considering that bayerite is the thermodynamically stable form of aluminum trihydroxide. Therefore, under the experimental conditions of pH 10 as reported during the electrochemical and surface characterization of the AA2024-T3 and AA2198-T8, bayerite is most likely formed on the surface of both alloys in the absence of lithium carbonate which chemical structure is also in line with the Raman bands reported in Fig. 10a and c respectively.

It has been demonstrated elsewhere [70] that the presence of lithium within an aqueous solution greatly limits the precipitation of pseudo-boehmite and selectively accelerates the pseudo-boehmite-to-bayerite transformation with relatively rapid kinetic phenomena to be involved. These rapid kinetic phenomena in the presence of lithium carbonate can potentially lead to the higher current densities observed in the polarization curves of AA2024-T3 (Fig. 2d) and AA2198-T8 (Fig. 3d) compared to the polarization curves obtained for the selected aluminum alloys in the absence of lithium carbonate. The transformation kinetics mentioned above are dominated by the pH and the concentration of aluminate and lithium in the aqueous solution. However, even though the presence of lithium is greatly affecting the formation of bayerite, it does not affect its thereafter growth properties [70]. Contrary to other alkali metals, lithium also co-precipitates with aluminum trihydroxide via intercalation into the structure [72] due to its significantly small ionic size thus decreasing the residual electron density of the aluminate polyhedron. As a result, the aluminate polyhedron adopts an increased tendency to act as an electron acceptor. Electroneutrality is achieved by the accumulation of negatively charged ions, usually carbonates, at the interlayer of the aluminum trihydroxide structure thus resulting into the formation of an Al-Li layered double hydroxide. For the initiation of this conversion process however it is a prerequisite to achieve supersaturation of the solution by $Al(OH)_4^-$ which is fulfilled through the direct dissolution of the aluminum matrix as described above [49].

For the formation of the Al-Li LDH it is important to preserve the pH of the aqueous solution at moderately alkaline conditions. The reactants for the aforementioned hydrotalcite-like compound are considered to be the aluminate ions, lithium ions and carbonate anions [17] for which their monomeric hydrolysis products are present in significant quantities in moderately alkaline aqueous solution. Assuming that the required local supersaturation is achieved, the conversion layer may form on the aluminum alloy matrix and respective intermetallic phases [49]. The formation of Al-Li LDH at the selected experimental conditions of pH 10 has been identified by Raman spectroscopy at 1065 cm^{-1} and 1063 cm^{-1} for AA2024-T3 (Fig. 10b) and AA2198-T8 (Fig. 10d) respectively. As revealed further by SEM characterization, the Al-Li LDH is uniformly formed on the surface of the selected aluminum alloys covering also the otherwise electrochemically active intermetallic phases. The presence of a distinct passive region in the anodic branch of AA2024-T3 (Fig. 2d) and AA2198-T8 (Fig. 3d) in the presence of lithium carbonate indicates the protective nature of the formed Al-Li LDH layer. The anodic dissolution of the aluminum matrix at the interface with the secondary intermetallic phase as observed by secondary SEM images (Fig. 9) suggests the importance of the aluminum matrix dissolution and supersaturation of solution with aluminate ions prior to the protective Al-Li LDH formation as also proposed by Kosari et al. [49]. Notable is the fact that greater anodic dissolution is observed for AA2198-T8 (Fig. 9d) for which the greater corrosion susceptibility [55] is proposed to be

associated with the presence of the T1 (Al_2CuLi) phase [33–36]. Consequently, the aforementioned argument regarding the importance of anodic dissolution in the formation of the protective layer is further supported.

Lastly, as discussed above, the aluminate ions are an integral part of the Al-Li LDH structure which offers corrosion protection on AA2024-T3 and AA2198-T8 at moderately alkaline conditions. However, the aluminate ions are thermodynamically unstable under acidic/near-neutral and strongly alkaline conditions due to the rapid monomeric hydrolysis of the aluminium aquo-cations in Al^{3+} and aluminum (hydr) oxide accordingly [46]. At low pH, amorphous structures are present instead of crystalline precipitates with the predominant hydrolyzed aluminum species to be 6-fold coordinated as opposed to the tetrahedral coordination of aluminum ions in alkaline pH [46]. However, at strongly alkaline pH the increased degree of hydrolysis of the aluminum species prevents possible precipitation into aluminum trihydroxide [73]. Consequently, a hydrotalcite-compound cannot be formed under the current strongly alkaline experimental conditions which also explains the lack of a passive behavior on the polarization curves of AA2024-T3 (Fig. 2a-c and e) and AA2198-T8 (Fig. 3a-c and e) at pH $\leq$ 7 and pH 13 [17].

5. Conclusions

It is demonstrated that lithium carbonate offers corrosion protection on both AA2024-T3 and AA2198-T8 under moderately alkaline conditions by the formation of a protective Al-Li LDH layer. The formation of this protective layer occurs through an active-to-passive transition which involves multiple stages. Initially the aluminum matrix undergoes anodic dissolution and once the required solution supersaturation with aluminate ions is achieved locally the conversion layer formation proceeds on the aluminum matrix and intermetallic phases. Even though the Al-Li LDH layer is formed on both AA2024-T3 and AA2198-T8, AA2198-T8 shows a higher susceptibility to anodic dissolution attributed to the T1 phase presence in the alloy matrix. Lastly, corrosion protection in the presence of lithium carbonate is only observed at moderately alkaline conditions. At acidic/near neutral and strongly alkaline aqueous solutions, the aluminate ion, which presence is a prerequisite to the conversion layer formation, is either not formed or is thermodynamically unstable. The hydrolysis kinetics of aluminum ions in acidic/near-neutral pH and the generation of aluminate ions in strongly alkaline pH result in insufficient solution supersaturation hindering the formation of the Al-Li LDH layer.

CRediT authorship contribution statement

E. Michailidou: Investigation, Writing – original draft, Writing – review & editing, **P. Visser:** Writing – review & editing, **J.M.C Mol:** Writing – review & editing, Supervision, **Kosari:** Investigation, Writing – review & editing, **H. Terryn:** Writing – review & editing, Supervision, **K. Baert:** Investigation, Writing – review & editing, **Y. Gonzalez-Garcia:** Writing – review & editing, Supervision.

Declaration of Competing Interest

The authors declare that they have no known competing financial interests or personal relationships that could have appeared to influence the work reported in this paper.

Data availability

Data will be made available on request.

Acknowledgment

This study was supported by the European research program Clean Sky 2. The ecoTECH Core Partner project has received funding from the European Union Horizon 2020 Clean Sky 2 Joint Undertaking under the AIRFRAME ITD grant agreement 945521 and the Transverse Activity ecoDESIGN grant agreement 945549.

Appendix A. Supporting information

Supplementary data associated with this article can be found in the online version at doi:10.1016/j.corsci.2022.110851.

References

[1] P. Visser, H. Terryn, J.M.C. Mol, On the importance of irreversibility of corrosion inhibitors for active coating protection of AA2024-T3, Corros. Sci. 140 (2018) 272–285, https://doi.org/10.1016/J.CORSCI.2018.05.037.
[2] P. Visser, K. Marcoen, G.F. Trindade, M.L. Abel, J.F. Watts, T. Hauffman, J.M. C. Mol, H. Terryn, The chemical throwing power of lithium-based inhibitors from organic coatings on AA2024-T3, Corros. Sci. 150 (2019) 194–206, https://doi.org/10.1016/J.CORSCI.2019.02.009.
[3] P. Visser, Y. Liu, X. Zhou, T. Hashimoto, G.E. Thompson, S.B. Lyon, L.G.J. van der Ven, A.J.M.C. Mol, H.A. Terryn, The corrosion protection of AA2024-T3 aluminium alloy by leaching of lithium-containing salts from organic coatings, Faraday Discuss. 180 (2015) 511–526, https://doi.org/10.1039/C4FD00237G.
[4] P. Visser, M. Meeusen, Y. Gonzalez-Garcia, H. Terryn, J.M.C. Mol, Electrochemical evaluation of corrosion inhibiting layers formed in a defect from lithium-leaching organic coatings, J. Electrochem Soc. 164 (2017) C396–C406, https://doi.org/10.1149/2.1411707JES/XML.
[5] P. Visser, A. Lutz, J.M.C. Mol, H. Terryn, Study of the formation of a protective layer in a defect from lithium-leaching organic coatings, Prog. Org. Coat. 99 (2016) 80–90, https://doi.org/10.1016/J.PORGCOAT.2016.04.028.
[6] P. Visser, Y. Gonzalez-Garcia, J.M.C. Mol, H. Terryn, Mechanism of passive layer formation on AA2024-T3 from alkaline lithium carbonate solutions in the presence of sodium chloride, J. Electrochem Soc. 165 (2018) C60–C70, https://doi.org/10.1149/2.1011802JES/XML.
[7] C.F. Baes, R.E. Mesmer, The hydrolysis of cations, Wiley, New York, 1976.
[8] W.M. Haynes, R. David, J. LideThomas, Bruno (Eds.), CRC Handbook of Chemistry and Physics, 97th ed., CRC Press, 2016 https://doi.org/10.1201/9781315380476.
[9] A. Kosari, F. Tichelaar, P. Visser, P. Taheri, H. Zandbergen, H. Terryn, J.M.C. Mol, Nanoscopic and in-situ cross-sectional observations of Li-based conversion coating formation using liquid-phase TEM, Npj Mater. Degrad. 2021 5:1 5 (2021) 1–9, https://doi.org/10.1038/s41529-021-00189-y.
[10] Y. Liu, P. Visser, X. Zhou, S.B. Lyon, T. Hashimoto, M. Curioni, A. Gholinia, G. E. Thompson, G. Smyth, S.R. Gibbon, D. Graham, J.M.C. Mol, H. Terryn, Protective Film Formation on AA2024-T3 Aluminum Alloy by Leaching of Lithium Carbonate from an Organic Coating, J. Electrochem Soc. 163 (2016) C45–C53, https://doi.org/10.1149/2.0021603JES/XML.
[11] Y. Liu, P. Visser, X. Zhou, S.B. Lyon, T. Hashimoto, A. Gholinia, G.E. Thompson, G. Smyth, S.R. Gibbon, D. Graham, J.M.C. Mol, H. Terryn, An investigation of the corrosion inhibitive layers generated from lithium oxalate-containing organic coating on AA2024-T3 aluminium alloy, Surf. Interface Anal. 48 (2016) 798–803, https://doi.org/10.1002/SIA.5972.
[12] K. Marcoen, P. Visser, G.F. Trindade, M.L. Abel, J.F. Watts, J.M.C. Mol, H. Terryn, T. Hauffman, Compositional study of a corrosion protective layer formed by leachable lithium salts in a coating defect on AA2024-T3 aluminium alloys, Prog. Org. Coat. 119 (2018) 65–75, https://doi.org/10.1016/J.PORGCOAT.2018.02.011.
[13] R. Buchheit, G. Stoner, Corrosion-Resistant, Chromate-Free Talc Coatings for Aluminum 8, CORROSION SCIENCE 205 CORROSION. 50 (n.d.).
[14] J.G. Craig, R.C. Newman, M.R. Jarrett, N.J.H. Holroyd, Local chemistry of stress-corrosion cracking in Al-Li-Cu-Mg alloys, Le. J. De. Phys. Colloq. 48 (1987) C3–825, https://doi.org/10.1051/JPHYSCOL:1987397.
[15] C.M. Rangel, M.A. Travassos, The passivation of aluminium in lithium carbonate/bicarbonate solutions, Corros. Sci. 33 (1992) 327–343, https://doi.org/10.1016/0010-938X(92)90064-A.
[16] J. Gui, T.M. Devine, Influence of lithium on the corrosion of aluminum, Scr. Metall. 21 (1987) 853–857, https://doi.org/10.1016/0036-9748(87)90336-X.
[17] R.G. Buchheit, F.D. Wall, G.E. Stoner, J.P. Moran, Anodic dissolution-based mechanism for the rapid cracking, preexposure phenomenon demonstrated by aluminum-lithium-copper alloys, Corrosion 51 (1995) 417–428, https://doi.org/10.5006/1.3293607.
[18] C.A. Drewien, M.O. Eatough, D.R. Tallant, C.R. Hills, R.G. Buchheit, Lithium-aluminum-carbonate-hydroxide hydrate coatings on aluminum alloys: composition, structure, and processing bath chemistry, J. Mater. Res 11 (1996) 1507–1513, https://doi.org/10.1557/JMR.1996.0188.
[19] H.N. McMurray, G. Williams, Under film/coating corrosion, Shreir's Corros. (2010) 988–1004, https://doi.org/10.1016/B978-044452787-5.00040-8.
[20] R.T. Ruggeri, T.R. Beck, An analysis of mass transfer in filiform corrosion, Corrosion 39 (1983) 452–465, https://doi.org/10.5006/1.3581907.
[21] J.L. Delplancke, S. Berger, X. Lefèbvre, D. Maetens, A. Pourbaix, N. Heymans, Filiform corrosion: interactions between electrochemistry and mechanical properties of the paints, Prog. Org. Coat. 43 (2001) 64–74, https://doi.org/10.1016/S0300-9440(01)00216-8.

[22] J.M.C. Mol, B.R.W. Hinton, D.H. van der Weijde, J.H.W. de Wit, S. van der Zwaag, A filiform corrosion and potentiodynamic polarisation study of some aluminium alloys, J. Mater. Sci. 2000 35:7 35 (2000) 1629–1639, https://doi.org/10.1023/A:1004795528090.

[23] T. Dorin, A. Vahid, J. Lamb, Aluminium lithium alloys, in: R.N. Lumley (Ed.), Fundamentals of Aluminium Metallurgy: Recent Advances, Woodhead Publishing, 2018, pp. 387–438, https://doi.org/10.1016/B978-0-08-102063-0.00011-4.

[24] R.J. Rioja, J. Liu, The evolution of Al-Li base products for aerospace and space applications, Met. Mater. Trans. A Phys. Met. Mater. Sci. 43 (2012) 3325–3337, https://doi.org/10.1007/S11661-012-1155-Z/FIGURES/19.

[25] N. Eswara Prasad, A.A. Gokhale, P. Rama Rao, Mechanical behaviour of aluminium-lithium alloys, Sadhana - Academy Proceedings in Engineering Sciences. 28 (2003) 209–246. https://doi.org/10.1007/BF02717134.

[26] R.J.H. Wanhill, N.E. Prasad, A.A. Gokhale, Aluminum-Lithium Alloys: Processing, Properties, and Applications, Butterworth-Heinemann,, 2013, https://doi.org/10.1016/C2012-0-00394-8.

[27] R.J.H. Wanhill, Status and prospects for aluminium-lithium alloys in aircraft structures, Int J. Fatigue 16 (1994) 3–20, https://doi.org/10.1016/0142-1123(94)90441-3.

[28] T. Warner, Recently-developed aluminium solutions for aerospace applications, Mater. Sci. Forum 519– 521 (2006) 1271–1278, https://doi.org/10.4028/WWW.SCIENTIFIC.NET/MSF.519-521.1271.

[29] J.A. Moreto, O. Gamboni, C.O.F.T. Rucherf, F. Romagnoli, M.F. Moreira, F. Beneduce, W.W.Bose Filho, Corrosion and fatigue behavior of new Al alloys, Procedia Eng. 10 (2011) 1521–1526, https://doi.org/10.1016/J.PROENG.2011.04.254.

[30] A. Boag, R.J. Taylor, T.H. Muster, N. Goodman, D. McCulloch, C. Ryan, B. Rout, D. Jamieson, A.E. Hughes, Stable pit formation on AA2024-T3 in a NaCl environment, Corros. Sci. 52 (2010) 90–103, https://doi.org/10.1016/J.CORSCI.2009.08.043.

[31] A.E. Hughes, R. Parvizi, M. Forsyth, Microstructure and corrosion of AA2024, Corros. Rev. 33 (2015) 1–30, https://doi.org/10.1515/CORRREV-2014-0039/XML.

[32] N. Birbilis, Y.M. Zhu, S.K. Kairy, M.A. Glenn, J.F. Nie, A.J. Morton, Y. Gonzalez-Garcia, H. Terryn, J.M.C. Mol, A.E. Hughes, A closer look at constituent induced localised corrosion in Al-Cu-Mg alloys, Corros. Sci. 113 (2016) 160–171, https://doi.org/10.1016/J.CORSCI.2016.10.018.

[33] U. Donatus, M. Terada, C.R. Ospina, F.M. Queiroz, A. Fatima Santos Bugarin, I. Costa, On the AA2198-T851 alloy microstructure and its correlation with localized corrosion behaviour, Corros. Sci. 131 (2018) 300–309, https://doi.org/10.1016/J.CORSCI.2017.12.001.

[34] J.V. de Sousa Araujo, U. Donatus, F.M. Queiroz, M. Terada, M.X. Milagre, M.C. de Alencar, I. Costa, On the severe localized corrosion susceptibility of the AA2198-T851 alloy, Corros. Sci. 133 (2018) 132–140, https://doi.org/10.1016/J.CORSCI.2018.01.028.

[35] B. Noble, G.E. Thompson, T 1 (Al2CuLi) Precipitation in Aluminium–Copper–Lithium Alloys, ⟨Http://Dx.Doi.Org/10.1179/030634572790445975⟩. 6 (2013) 167–174. ⟨https://doi.org/10.1179/030634572790445975⟩.

[36] R.G. Buchheit, J.P. Moran, G.E. Stoner, Localized corrosion behavior of alloy 2090—the role of microstructural heterogeneity, Corrosion 46 (1990) 610–617, https://doi.org/10.5006/1.3585156.

[37] M.Q.Ian Polmear, David St John, Jian-Feng Nie, Light Alloys; Sectĩon-2 Physical Metallurgy of Aluminium Alloys, Butterworth-Heinemann,, 2017.

[38] R.G. Buchheit, M.A. Martinez, L.P. Montes, Evidence for Cu Ion Formation by Dissolution and Dealloying the Al[sub 2]CuMg Intermetallic Compound in Rotating Ring-Disk Collection Experiments, J. Electrochem Soc. 147 (2000) 119, https://doi.org/10.1149/1.1393164/XML.

[39] R.G. Buchheit, J.P. Moran, G.E. Stoner, Electrochemical behavior of the T1 (Al2CuLi) intermetallic compound and its role in localized corrosion of Al-2% Li-3% Cu alloys, Corrosion 50 (1994) 120–130. ⟨https://doi.org/10.5006/1.3293500⟩.

[40] V. Proton, J. Alexis, E. Andrieu, J.Ô. Delfosse, A. Deschamps, F. de Geuser, M. C. Lafont, C. Blanc, The influence of artificial ageing on the corrosion behaviour of a 2050 aluminium–copper–lithium alloy, Corros. Sci. 80 (2014) 494–502, https://doi.org/10.1016/J.CORSCI.2013.11.060.

[41] C.R. Bryan, A.W. Knight, R.M. Katona, A.C. Sanchez, E.J. Schindelholz, R. F. Schaller, Physical and chemical properties of sea salt deliquescent brines as a function of temperature and relative humidity, Sci. Total Environ. 824 (2022), 154462, https://doi.org/10.1016/J.SCITOTENV.2022.154462.

[42] J. Sullivan, S. Mehraban, J. Elvins, In situ monitoring of the microstructural corrosion mechanisms of zinc–magnesium–aluminium alloys using time lapse microscopy, Corros. Sci. 53 (2011) 2208–2215, https://doi.org/10.1016/J.CORSCI.2011.02.043.

[43] K.A. Unocic, M.J. Mills, G.S. Daehn, Effect of gallium focused ion beam milling on preparation of aluminium thin foils, J. Microsc. 240 (2010) 227–238, https://doi.org/10.1111/J.1365-2818.2010.03401.X.

[44] R. Stumpf, P.J. Feibelman, Towards an understanding of liquid-metal embrittlement: energetics of ga on Al surfaces, Phys. Rev. B. 54 (1996) 5145, https://doi.org/10.1103/PhysRevB.54.5145.

[45] J.A. Moreto, C.E.B. Marino, W.W. Bose Filho, L.A. Rocha, J.C.S. Fernandes, SVET, SKP and EIS study of the corrosion behaviour of high strength Al and Al–Li alloys used in aircraft fabrication, Corros. Sci. 84 (2014) 30–41, https://doi.org/10.1016/J.CORSCI.2014.03.001.

[46] M. Pourbaix, Atlas of electrochemical equilibria in aqueous solutions, [1st English ed.], Pergamon Press,, Oxford;New York, 1966.

[47] N. Wint, Z.S. Barrett, G. Williams, H.N. McMurray, The study of AA2024 De-alloying using luminol electrogenerated chemiluminescence imaging, J. Electrochem Soc. 166 (2019) C3417–C3430, https://doi.org/10.1149/2.0481911JES/XML.

[48] R.T. Lowson, Aluminium corrosion studies. IV. Pitting corrosion, Aust. J. Chem. 31 (1978) 943–956, https://doi.org/10.1071/CH9780943.

[49] A. Kosari, F. Tichelaar, P. Visser, H. Zandbergen, H. Terryn, J.M.C. Mol, Laterally-resolved formation mechanism of a lithium-based conversion layer at the matrix and intermetallic particles in aerospace aluminium alloys, Corros. Sci. 190 (2021), 109651, https://doi.org/10.1016/J.CORSCI.2021.109651.

[50] A. Kosari, F. Tichelaar, P. Visser, H. Zandbergen, H. Terryn, J.M.C. Mol, Dealloying-driven local corrosion by intermetallic constituent particles and dispersoids in aerospace aluminium alloys, Corros. Sci. 177 (2020), 108947, https://doi.org/10.1016/J.CORSCI.2020.108947.

[51] A. Kosari, P. Visser, F. Tichelaar, S. Eswara, J.N. Audinot, T. Wirtz, H. Zandbergen, H. Terryn, J.M.C. Mol, Cross-sectional characterization of the conversion layer formed on AA2024-T3 by a lithium-leaching coating, Appl. Surf. Sci. 512 (2020), 145665, https://doi.org/10.1016/J.APSUSC.2020.145665.

[52] L. Lacroix, L. Ressier, C. Blanc, G. Mankowski, Statistical study of the corrosion behavior of Al2CuMg intermetallics in AA2024-T351 by SKPFM, J. Electrochem Soc. 155 (2008) C8, https://doi.org/10.1149/1.2799089/XML.

[53] A. Kosari, H. Zandbergen, F. Tichelaar, P. Visser, P. Taheri, H. Terryn, J.M.C. Mol, In-situ nanoscopic observations of dealloying-driven local corrosion from surface initiation to in-depth propagation, Corros. Sci. 177 (2020), 108912, https://doi.org/10.1016/J.CORSCI.2020.108912.

[54] L. Lacroix, L. Ressier, C. Blanc, G. Mankowski, Combination of AFM, SKPFM, and SIMS to study the corrosion behavior of S-phase particles in AA2024-T351, J. Electrochem Soc. 155 (2008) C131, https://doi.org/10.1149/1.2833315/XML.

[55] A.F.S. Santos, S. Zacarelli, M. Terada, I. Costa, Effect of microstructure on the corrosion resistance of AA2524-T3 and AA2198-T851 aluminum alloys used in the aeronautic industry, Eur. Corros. Congr. 82 (2014) 82–97.

[56] Y. Ma, X. Zhou, Y. Liao, Y. Yi, H. Wu, Z. Wang, W. Huang, Localised corrosion in AA 2099-T83 aluminium-lithium alloy: the role of grain orientation, Corros. Sci. 107 (2016) 41–48, https://doi.org/10.1016/J.CORSCI.2016.02.018.

[57] Y. Ma, X. Zhou, W. Huang, Y. Liao, X. Chen, X. Zhang, G.E. Thompson, Crystallogr. Defects Induc. Local. Corros. AA2099-T8 Alum. Alloy 50 (2014) 420–424. ⟨https://doi.org/10.1179/1743278214Y.0000000237⟩.

[58] J.E. Kertz, P.I. Gouma, R.G. Buchheit, Localized corrosion susceptibility of Al-Li-Cu-Mg-Zn alloy AF/C458 due to interrupted quenching from solutionizing temperature, Metall. Mater. Trans. A 2001 32:10 32 (2001) 2561–2573, https://doi.org/10.1007/S11661-001-0046-5.

[59] P. Hovington, V. Timoshevskii, S. Burgess, P. Statham, H. Demers, R. Gauvin, K. Zaghib, Towards Li quantification at high spatial resolution using EDS, Microsc. Microanal. 22 (2016) 84–85, https://doi.org/10.1017/S1431927616001276.

[60] P. Hovington, V. Timoshevskii, S. Bessette, S. Burgess, P. Statham, H. Demers, R. Gauvin, K. Zaghib, On the detection limits of Li K X-rays using windowless energy dispersive spectrometer (EDS, Microsc. Microanal. 23 (2017) 2024–2025, https://doi.org/10.1017/S1431927617010789.

[61] H.D. Ruan, R.L. Frost, J.T. Kloprogge, Comparison of Raman spectra in characterizing gibbsite, bayerite, diaspore and boehmite, J. Raman Spectrosc. 32 (2001) 745–750, https://doi.org/10.1002/JRS.736.

[62] J. Guo, Z. Wang, J. Cao, X. Gong, Structures of solvated tetramethylammonium aluminate species and its transformation mechanism by DFT and Raman spectra, J. Mol. Struct. 1199 (2020), 126791, https://doi.org/10.1016/J.MOLSTRUC.2019.07.038.

[63] A. Balbo, A. Frignani, V. Grassi, F. Zucchi, Electrochemical behaviour of AA2198 and AA2139 in neutral solutions, Mater. Corros. 66 (2015) 796–802, https://doi.org/10.1002/MACO.201408059.

[64] R.G. Buchheit, R.P. Grant, P.F. Hlava, B. Mckenzie, G.L. Zender, Local dissolution phenomena associated with S phase (Al2CuMg) particles in aluminum alloy 2024–T3, J. Electrochem Soc. 144 (1997) 2621–2628, https://doi.org/10.1149/1.1837874/XML.

[65] T.J.R. Leclère, R.C. Newman, Self-regulation of the cathodic reaction kinetics during corrosion of AlCu alloys, J. Electrochem Soc. 149 (2002) B52, https://doi.org/10.1149/1.1432669/XML.

[66] N. Dimitrov, J.A. Mann, M. Vukmirovic, K. Sieradzki, Dealloying of Al[sub 2]CuMg in Alkaline Media, J. Electrochem Soc. 147 (2000) 3283, https://doi.org/10.1149/1.1393896/XML.

[67] G. Sposito, The Environmental Chemistry of Aluminum, Second Edition, 1995. ⟨https://www.routledge.com/The-Environmental-Chemistry-of-Aluminum/Sposito/p/book/9781566700306⟩ (accessed May 18, 2022).

[68] S. il Pyun, S.M. Moon, Corrosion mechanism of pure aluminium in aqueous alkaline solution, J. Solid State Electrochem. 4 (2000) 267–272, https://doi.org/10.1007/s100080050203.

[69] S.M. Moon, S.I. Pyun, The corrosion of pure aluminium during cathodic polarization in aqueous solutions, Corros. Sci. 39 (1997) 399–408, https://doi.org/10.1016/S0010-938X(97)83354-9.

[70] H.A. van Straten, M.A.A. Schoonen, P.L. de Bruyn, Precipitation from supersaturated aluminate solutions. III. Influence of alkali ions with special reference to Li+, J. Colloid Interface Sci. 103 (1985) 493–507, https://doi.org/10.1016/0021-9797(85)90125-0.

[71] H.A. van Straten, B.T.W. Holtkamp, P.L. de Bruyn, Precipitation from supersaturated aluminate solutions: I. Nucleation and growth of solid phases at

room temperature, J. Colloid Interface Sci. 98 (1984) 342–362, https://doi.org/10.1016/0021-9797(84)90159-0.

[72] M. Frenkel, A. Glasner, S. Sarig, Crystal modification of freshly precipitated aluminum hydroxide by lithium ion intercalation, J. Phys. Chem. 84 (1980) 507–510, https://doi.org/10.1021/J100442A010/ASSET/J100442A010.FP.PNG_V03.

[73] B.H.W.S. de Jong, C.M. Schramm, V.E. Parziale, Polymerization of silicate and aluminate tetrahedra in glasses, melts, and aqueous solutions—IV. Aluminum coordination in glasses and aqueous solutions and comments on the aluminum avoidance principle, Geochim Cosmochim. Acta 47 (1983) 1223–1236, https://doi.org/10.1016/0016-7037(83)90064-9.